Separation and Purification Technology 393 (2026) 137266

Contents lists available at ScienceDirect

Separation and Purification Technology

journal homepage: www.elsevier.com/locate/seppur

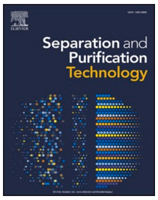

# Synthesis of a novel *Z*-scheme $CeVO_4/Bi_2Sn_2O_7$ heterojunction with dual photocatalytic functionality for $CO_2$ conversion and pharmaceutical pollutant degradation

Rahila Batul [a], Ali B.M. Ali [b], Mohamed A. Ismail [c], Pradeep Kumar Singh [d,*], Shatha A. Aldaghfag [e], Ibrahm Mahariq [f,g,*], Bakhodir Saydullaev [h], Miyribek Seytnazarov [i], Mukhtorjon Karimov [j], Reda A. Haggam [k,*]

[a] *Department of Pharmaceutical Chemistry, College of pharmacy, University of Hail, Saudi Arabia*
[b] *Advanced Technical College, University of Warith Al-Anbiyaa, Karbala, Iraq*
[c] *Department of Chemical Engineering, College of Engineering, King Khalid University, Abha 61411, Saudi Arabia*
[d] *Department of Mechanical Engineering, Institute of Engineering & Technology, GLA University, Mathura, Uttar Pradesh 281406, India*
[e] *Department of Physics, College of Sciences, Princess Nourah bint Abdulrahman University, P. O. Box 84428, Riyadh 11671, Saudi Arabia*
[f] *University College, Korea University, Seoul 02481, South Korea*
[g] *Department of Medical Research, China Medical University Hospital, China Medical University, Taichung, Taiwan*
[h] *The Department of Pharmaceutical and Chemistry, Alfraganus University, Yukori Karakamish street 2a, Tashkent 100190, Uzbekistan*
[i] *Kimyo International University in Tashkent, Shota Rustaveli str. 156, Tashkent 100121, Uzbekistan*
[j] *Urgench State University, 14, Kh. Alimdjan str, Urgench 220100, Uzbekistan*
[k] *Department of Chemistry, Faculty of Science, Islamic University of Madinah, Madinah 42351, Saudi Arabia*

ARTICLE INFO

Editor: Yeshui Zhang

*Keywords:*
Z-scheme heterojunction
$CeVO_4/Bi_2Sn_2O_7$
Photocatalytic $CO_2$ reduction
Antibiotic degradation
Density functional theory (DFT)
Wastewater treatment

ABSTRACT

The simultaneous mitigation of antibiotic pollution and greenhouse gas $CO_2$ represents a critical yet challenging goal for sustainable environmental technology. This study reports the rational development of a new direct *Z*-scheme $CeVO_4/Bi_2Sn_2O_7$ heterojunction fabricated through a straightforward, well-controlled hydrothermal–ultrasonication strategy, and demonstrates its dual-function photocatalytic performance. Comprehensive characterization confirms the formation of an intimate interface between n-type $CeVO_4$ and p-type $Bi_2Sn_2O_7$, which facilitates a direct Z-scheme charge-transfer mechanism. This unique configuration effectively suppresses electron-hole recombination while preserving high redox potentials, as validated by photoelectrochemical measurements, ESR, and radical trapping experiments. The optimized 30 wt% $CeVO_4/Bi_2Sn_2O_7$ composite exhibits exceptional performance, achieving a visible-light $CO_2$ reduction rate of 5.17 $\mu mol\ g^{-1}\ h^{-1}$ for CO and 3.96 $\mu mol\ g^{-1}\ h^{-1}$ for $CH_4$, which corresponds to 11.5-fold and 19.8-fold enhancements over pristine $CeVO_4$, respectively. Concurrently, the composite degrades 98.18% of sulfamethoxazole (SMX), with a mineralization efficiency of 81.46% and a significant reduction in ecotoxicity of the byproducts. The catalyst demonstrates outstanding stability over four cycles, broad-spectrum activity against various antibiotics, and robust performance in complex water matrices, including tap and real wastewater. Density Functional Theory (DFT) calculations elucidate the reactive sites on the SMX molecule, corroborating the proposed degradation pathways. This study provides a mechanistic blueprint for developing efficient *Z*-scheme heterostructures, positioning the $CeVO_4/Bi_2Sn_2O_7$ photocatalyst as a promising platform for integrated environmental remediation and solar fuel production.

## 1. Introduction

The growing concentration of carbon dioxide ($CO_2$) in the atmosphere, primarily driven by industrialization and the burning of fossil fuels, has become a central environmental issue [1,2]. $CO_2$ is a significant greenhouse gas that contributes to global warming, ocean acidification, and the broader climate change crisis [3]. This escalating environmental threat highlights the urgent need for effective strategies

---

* Corresponding authors.
*E-mail addresses:* pradeep.kumar@gla.ac.in (P.K. Singh), lbmmahariq@gmail.com (I. Mahariq), relhaggan@iu.edu.sa (R.A. Haggam).

https://doi.org/10.1016/j.seppur.2026.137266
Received 28 November 2025; Received in revised form 22 January 2026; Accepted 11 February 2026

to mitigate $CO_2$ emissions and convert it into valuable products [4]. In this context, the photocatalytic conversion of $CO_2$ into valuable chemicals CO, $CH_4$, and other C2+ products has garnered considerable attention [5]. These technologies present a promising solution to reduce carbon emissions while simultaneously contributing to sustainable industrial practices. On the other hand, sulfonamide antibiotics, especially SMX, are widely used to treat bacterial infections in humans and animals [6]. However, SMX persists in the environment, posing risks to aquatic ecosystems and human health. A large proportion is excreted unchanged and enters water bodies via wastewater, where it accumulates at detectable levels, such as 1.468 μg/L in the Yangtze River Basin. Despite conventional treatment, removal efficiencies are often below 30%, leading to bioaccumulation and potential disruption of aquatic life [7,8]. The persistence of SMX can also promote antibiotic resistance and pose long-term health risks to humans through contaminated water. Therefore, developing efficient photocatalytic systems to remove SMX while simultaneously facilitating $CO_2$ conversion is an urgent priority for environmental health.

Conventional wastewater treatment approaches—including ozonation [9], chlorination [10], adsorption [11], and membrane filtration [12] —are widely used, yet they often suffer from drawbacks such as elevated operating expenses, lengthy processing durations, and the production of secondary sludge [13–15]. These shortcomings highlight the need for more efficient and next-generation treatment strategies. In this context, advanced oxidation processes (AOPs) have attracted increasing attention as effective routes for breaking down recalcitrant organic contaminants, including SMX [16,17]. AOPs involve generating highly reactive radicals and other reactive oxygen species (ROS) that effectively break down organic contaminants in water. Photocatalysis, as a form of AOP, is particularly effective in wastewater treatment [18,19]. This process utilizes solar energy to generate electron-hole pairs in photocatalysts, which subsequently participate in redox reactions to degrade pollutants [20,21]. At the same time, photocatalytic $CO_2$ reduction is gaining significant attention as a sustainable approach to address the global $CO_2$ emissions crisis [22]. Unlike thermocatalytic and electrocatalytic methods, which require high temperatures or external power sources, photocatalysis operates under mild conditions using only solar energy [23–25]. This makes it a promising candidate for large-scale $CO_2$ conversion processes. However, single-component photocatalysts often face challenges such as poor charge separation, limited redox potential, and low solar-to-chemical conversion efficiency. These drawbacks result in rapid electron-hole recombination, which leads to energy losses and poor catalytic performance. Moreover, traditional systems struggle to achieve both effective light absorption and the necessary redox potentials to drive the $CO_2$ reduction process, limiting their practical applications.

To overcome these limitations, the development of heterojunction photocatalysts, such as type-II, *Z*-scheme, and S-scheme systems, has gained attention for their ability to enhance charge separation and improve photocatalytic efficiency [26–28]. While type-II heterojunctions effectively promote charge separation, they compromise redox potential due to the unbalanced distribution of photogenerated carriers [29,30]. Conversely, S-scheme systems maintain high redox potentials but suffer from inefficient charge transfer, leading to suboptimal performance. The recently proposed *Z*-scheme heterojunction addresses both limitations by enabling selective recombination of low-energy carriers while preserving the strong redox capabilities of the high-energy carriers [31–33]. This mechanism significantly enhances the photocatalytic performance for both pollutant degradation and $CO_2$ reduction, making it an ideal strategy for improving photocatalytic efficiency under visible light.

Cerium vanadate ($CeVO_4$), with its narrow band gap and strong redox activity, has attracted significant interest as a photocatalyst. The $Ce^{3+}/Ce^{4+}$ redox pair further enhances charge carrier mobility, making $CeVO_4$ an effective candidate for photocatalytic reactions [34]. However, its photocatalytic performance is often limited by rapid electron-hole recombination, moderate light absorption, and a relatively low specific surface area [35]. To enhance the performance of $CeVO_4$, several composites have been developed, including $CeVO_4$/MIL-88 [36], $CeVO_4/TiO_2/SnS$ [37], and $n_2S_3$-$CeVO_4$-$La_2O_3$ [38], which improve charge transfer and enhance photocatalytic activity. Similarly, $Bi_2Sn_2O_7$, a promising p-type semiconductor, exhibits excellent oxidative potential but suffers from poor electrical conductivity and fast charge recombination [39,40]. Hybrid structures involving $Bi_2Sn_2O_7$, such as $AgI/Bi_2Sn_2O_7$ [41] and $Bi_2Sn_2O_7/ZnIn_2S_4$ [42], have demonstrated enhanced photoactivity by improving charge separation and light utilization. It's to be noted that, $CeVO_4$ and $Bi_2Sn_2O_7$ were selected based on a complementary, mechanism-driven design for dual photocatalysis. $CeVO_4$ is a visible-light-active vanadate in which the $Ce^{3+}/Ce^{4+}$ redox couple and defect-tolerant lattice can promote interfacial charge transport and surface redox cycling, offering a suitable oxidation-side component for antibiotic degradation. Nevertheless, pristine $CeVO_4$ typically suffers from rapid electron–hole recombination and limited carrier utilization, which restricts its standalone activity. In parallel, $Bi_2Sn_2O_7$ is a chemically robust bismuth-based oxide (often reported as p-type) whose electronic structure can support efficient electron participation, yet its practical performance is frequently limited by low conductivity and fast recombination. Coupling these two oxides is therefore expected to create a built-in electric field and a tightly contacted interface that promotes directional charge separation while maintaining strong redox capability, which is essential for simultaneously driving oxidative SMX degradation and reductive $CO_2$ conversion under visible light. The combination of $CeVO_4$ and $Bi_2Sn_2O_7$ into a *Z*-scheme structure is anticipated to effectively overcome the limitations of both materials, leading to more efficient charge separation and enhanced photocatalytic activity.

Here, we describe the rational development and fabrication of a new direct Z-scheme $CeVO_4/Bi_2Sn_2O_7$ heterojunction using a convenient, well-controlled hydrothermal–ultrasonication approach. The study investigates its dual-function photocatalytic performance for simultaneous visible-light-driven degradation of SMX in water and $CO_2$ reduction. The synergistic interplay between n-type $CeVO_4$ and p-type $Bi_2Sn_2O_7$ was meticulously investigated through a suite of physicochemical, electrochemical, and spectroscopic techniques. Furthermore, the charge-transfer mechanism and the pathways for SMX degradation were elucidated through radical trapping experiments, electron spin resonance (ESR), and Density Functional Theory (DFT) calculations. The catalyst's practical applicability was assessed through reusability tests, mineralization efficiency (TOC), toxicity evaluation of transformation products, and performance across various antibiotic pollutants and water matrices. This study provides a comprehensive mechanistic insight into the functioning of a $CeVO_4/Bi_2Sn_2O_7$ *Z*-scheme heterojunction, presenting it as a robust and versatile photocatalyst for addressing intertwined environmental and energy challenges.

## 2. Materials and methods

### 2.1. Chemicals and materials

All reagents used in this work were of analytical grade and utilized without additional purification. Cerium nitrate hexahydrate [$Ce(NO_3)_3 \cdot 6H_2O$] and ammonium metavanadate ($NH_4VO_3$) served as precursor salts for synthesizing $CeVO_4$, while bismuth nitrate pentahydrate [$Bi(NO_3)_3 \cdot 5H_2O$] and tin(IV) chloride pentahydrate [$SnCl_4 \cdot 5H_2O$] were employed for $Bi_2Sn_2O_7$ preparation. Urea ($CO(NH_2)_2$) and sodium hydroxide (NaOH) were used as precipitating and pH-controlling agents during hydrothermal processing. SMX was chosen as the model antibiotic pollutant due to its persistence and environmental relevance. Ethanol (≥99.8%) and deionized water (DI) were used as solvents for washing, dispersion, and all aqueous preparations.

### 2.2. Preparation of n-type $CeVO_4$ photocatalyst

Pure $CeVO_4$ nanoparticles were synthesized through a controlled hydrothermal route. In a standard procedure, aqueous solutions of cerium nitrate hexahydrate [$Ce(NO_3)_3 \cdot 6H_2O$, 0.2 M] and ammonium metavanadate ($NH_4VO_3$, 0.1 M) were separately prepared under continuous magnetic stirring (Schematic 1). The $NH_4VO_3$ solution was gradually introduced into the $Ce(NO_3)_3$ solution, resulting in a visible color shift from pale yellow to golden within approximately 10 min, which indicated the onset of complex formation between $Ce^{3+}$ and $VO_4^{3-}$ species. To modulate nucleation kinetics and facilitate uniform crystal formation, urea (0.1 M) was introduced as a gentle chelating/stabilizing additive. The suspension was further stirred for 30 min to ensure thorough precursor dispersion. The resulting homogeneous sol was then loaded into a Teflon-lined stainless-steel autoclave and heated at 180 °C for 12 h under static conditions. After cooling naturally to room temperature, the yellow solid was separated by centrifugation, repeatedly washed with absolute ethanol and deionized water to eliminate residual species, and dried at 80 °C overnight. The final product was highly crystalline $CeVO_4$ nanoparticles.

### 2.3. Preparation of p-type $bi_2Sn_2O_7$ photocatalyst

$Bi_2Sn_2O_7$ nanoparticles were prepared through a simple one-step hydrothermal synthesis. Typically, stoichiometric quantities of bismuth nitrate pentahydrate [$Bi(NO_3)_3 \cdot 5H_2O$] and tin(IV) chloride pentahydrate [$SnCl_4 \cdot 5H_2O$] were individually dissolved in 30 mL of deionized water under constant stirring for 25 min. To ensure complete dissolution of $Bi^{3+}$ ions, a small volume of nitric acid ($HNO_3$) was slowly added until a transparent solution was obtained (Schematic 1). The two precursor solutions were then combined dropwise under continuous stirring for 30 min to form a uniform sol. The pH of the resulting mixture was carefully adjusted to about 8 using a 1 M NaOH solution. Subsequently, the mixture was sealed in a 100 mL Teflon-lined autoclave and subjected to hydrothermal treatment at 180 °C for 12 h. After cooling, the yellow precipitate was separated by centrifugation, washed repeatedly with deionized water and ethanol to remove residual ions, and dried at 80 °C for 12 h. The resulting fine powder was lightly ground using an agate mortar to yield homogeneous $Bi_2Sn_2O_7$ nanoparticles with uniform morphology and high purity.

### 2.4. Fabrication of Z-scheme $CeVO_4/bi_2Sn_2O_7$ heterojunction

The Z-scheme $CeVO_4/Bi_2Sn_2O_7$ heterostructured photocatalysts were fabricated using a straightforward water-based dispersion followed by ultrasonication. Typically, a predetermined amount of the prepared $Bi_2Sn_2O_7$ powder was dispersed in 150 mL of deionized water and magnetically stirred for 20 min to form a stable suspension. Then, an appropriate mass of $CeVO_4$ nanoparticles was added to obtain a series of composites with different loadings (10, 20, 30, and 40 wt% with respect to $Bi_2Sn_2O_7$). The resulting composites were designated as x-$CeVO_4/Bi_2Sn_2O_7$ ($x = 10, 20, 30, 40$ wt%). Each dispersion was kept under dark stirring for 20 min, followed by 40 min of ultrasonication to promote intimate interfacial contact between $CeVO_4$ and $Bi_2Sn_2O_7$ and to facilitate the in-situ formation of a *Z*-scheme charge transfer junction. The mixture was further stirred for an additional 30 min to stabilize the suspension. The products were subsequently filtered, vacuum-dried at 80 °C overnight, and stored for subsequent characterization and photocatalytic studies.

### 2.5. Photocatalytic degradation of sulfamethoxazole pollutant

The photocatalytic performance of the prepared materials was evaluated using the degradation of SMX as a model contaminant under visible-light irradiation. A 100 mL aqueous SMX solution (5 mg $L^{-1}$) was prepared in deionized water and mixed with 50 mg of photocatalyst in a quartz reactor equipped with continuous stirring. Prior to illumination, the suspension was stirred in the dark for 30 min to establish adsorption–desorption equilibrium between SMX molecules and the catalyst surface. Subsequently, the reaction mixture was irradiated using a 300 W Xe lamp fitted with a 420 nm cutoff filter to ensure visible-light excitation. At defined time intervals, 5 mL aliquots were withdrawn, centrifuged at 8000 rpm for 10 min, and filtered through 0.45 μm glass microfiber filters to remove catalyst residues. The residual concentration of SMX was monitored via UV–Vis spectrophotometry at its characteristic absorption wavelength ($\lambda_{max} \approx 266$ nm). Additionally, total organic carbon (TOC) analysis was conducted to evaluate the extent of mineralization, providing a more comprehensive assessment of pollutant removal efficiency.

### 2.6. Photocatalytic $CO_2$ reduction

Photocatalytic $CO_2$ conversion experiments were conducted in a

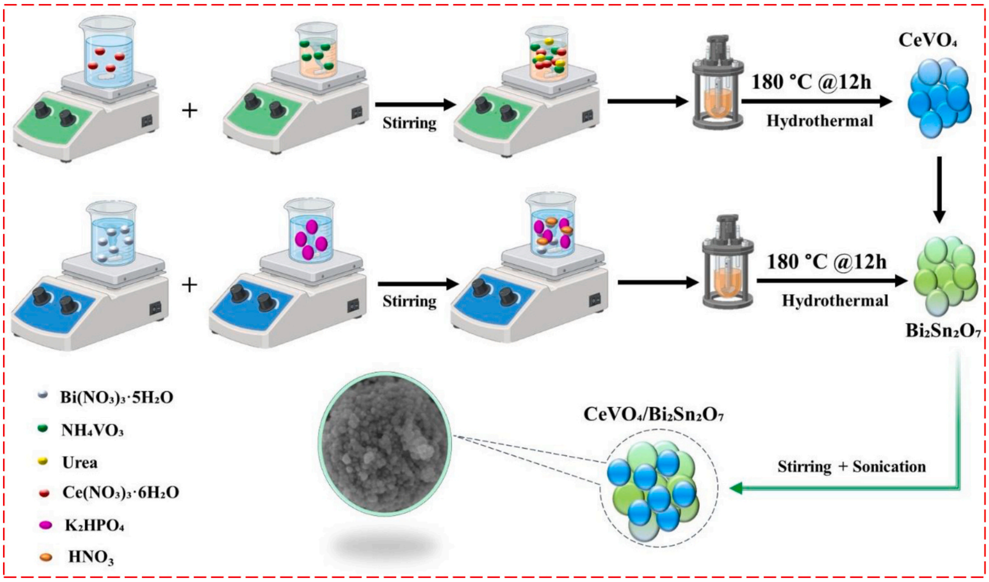

**Schematic 1.** Schematic of the preparation of the catalysts.

sealed 25 mL Pyrex reactor under visible-light irradiation. In a typical test, 3 mg of photocatalyst was dispersed in 40 μL of deionized water to act as the proton donor. The reactor was initially evacuated to remove residual air, then purged with ultra-high-purity $CO_2$ (99.999%) for 40 min to achieve a saturated $CO_2$ environment. Illumination was provided by a 300 W Xe arc lamp equipped with a 400 nm long-pass optical filter, simulating visible-light conditions. The incident light intensity was adjusted to 100 mW $cm^{-2}$ using a calibrated silicon photodiode to ensure consistent irradiance. After the reaction, the evolved gaseous products were analyzed using a SHIMADZU GC-2014 gas chromatograph equipped with a flame ionization detector and methanizer, allowing for quantitative detection of $CO_2$ reduction products such as CO, $CH_4$.

### 2.7. Characterization techniques

A comprehensive suite of physicochemical analyses was performed to elucidate the structural, morphological, optical, and electronic characteristics of the synthesized photocatalysts. The crystalline phases were examined using X-ray diffraction (XRD, Bruker D8 Advance, Cu Kα radiation, λ = 1.5406 Å) to determine phase composition, lattice parameters, and crystallite sizes. Morphological features were analyzed via scanning electron microscopy (SEM, Hitachi Regulus 8230) and transmission electron microscopy (TEM, JEOL JEM-2100), while high-

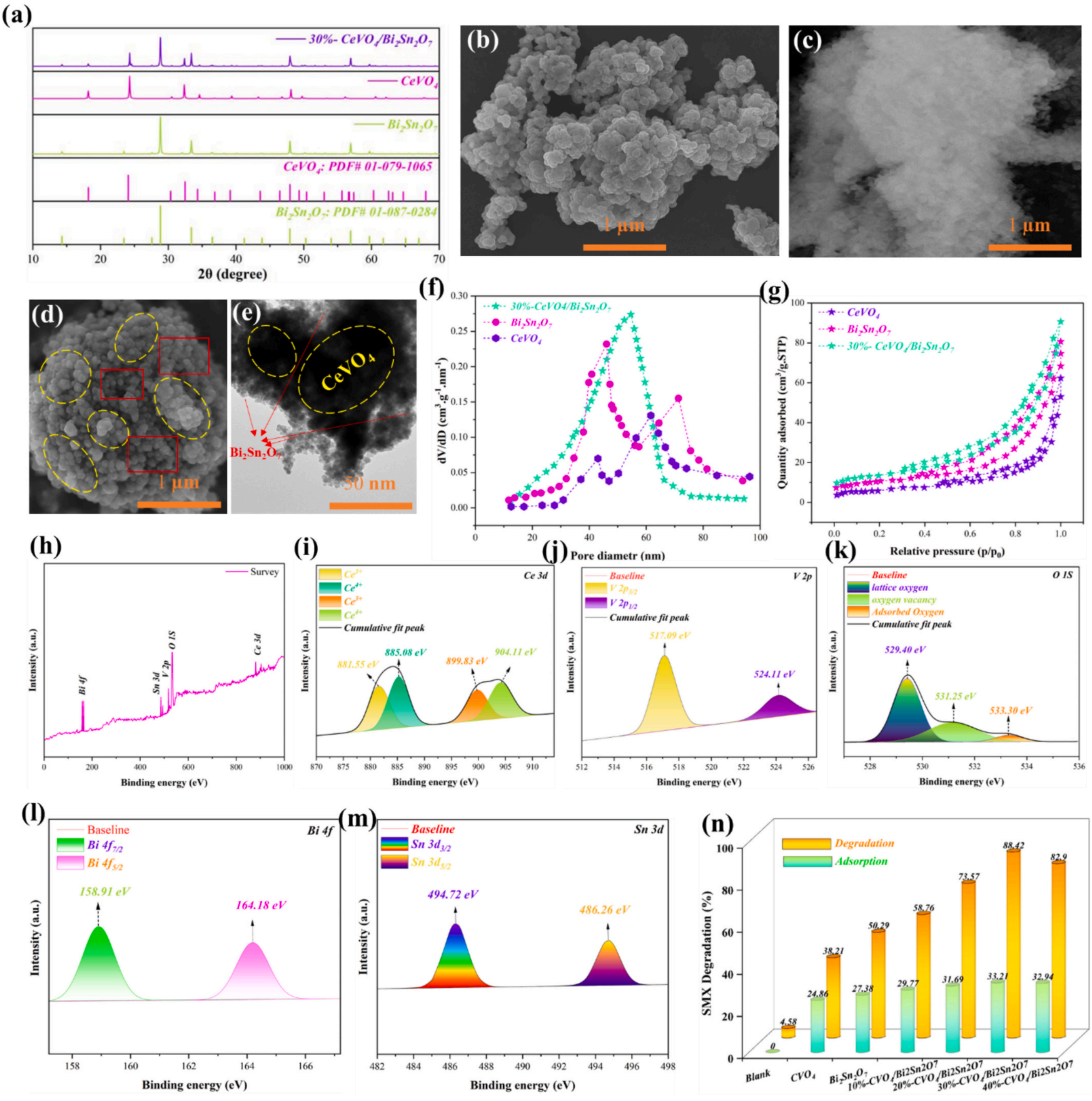

**Fig. 1.** Structural, morphological and surface characterization of the synthesized photocatalysts: (a) XRD patterns, (b–c) SEM images of $CeVO_4$ and $Bi_2Sn_2O_7$, (d–e) SEM and TEM images of 30 wt% $CeVO_4/Bi_2Sn_2O_7$, (f–g) BJH pore-size dsistribution and $N_2$ adsorption–desorption isotherms, (h–m) XPS spectra of $CeVO_4/Bi_2Sn_2O_7$ (survey, Ce 3d, V 2p, O 1 s, Bi 4f, Sn 3d), and (n) SMX adsorption and degradation efficiencies under visible light.

resolution TEM (HR-TEM) provided interplanar spacing and lattice-fringe details, confirming intimate junction formation. The elemental makeup and corresponding oxidation (valence) states were examined using X-ray photoelectron spectroscopy (XPS; Thermo Fisher ESCALAB 250Xi). Optical light-harvesting behavior was evaluated via UV–Vis diffuse reflectance spectroscopy (Shimadzu UV-2600), and the optical bandgap values were derived from Tauc-plot analysis. The Brunauer–Emmett–Teller (BET) method was applied to nitrogen adsorption–desorption isotherms (Micromeritics ASAP 2020) to estimate surface area, pore volume, and pore size distribution. Photoluminescence (PL) and time-resolved PL (TRPL) measurements were carried out to investigate the recombination behavior and lifetimes of photoinduced charge carriers. Electrochemical impedance spectroscopy (EIS) and transient photocurrent measurements were conducted using a CHI660E workstation in a standard three-electrode setup to evaluate charge transfer resistance and interfacial carrier dynamics.

### 2.8. *Density functional theory (DFT) calculations*

Density functional theory (DFT) simulations were performed using the DMol$^3$ module in Materials Studio 2024 to elucidate the electronic properties and reactivity of SMX. Geometry optimization employed the PBE functional under the GGA framework with a DNP basis set and DSPP treatment for heavy atoms. Convergence thresholds were $1 \times 10^{-6}$ Ha (energy), $1 \times 10^{-5}$ Ha·Å$^{-1}$ (forces), and $5 \times 10^{-4}$ Å (displacements). Frequency analysis confirmed the absence of imaginary modes. Frontier orbital distributions (HOMO and LUMO), electrostatic potential (ESP) maps, Hirshfeld charge populations, and condensed Fukui indices ($f^+$, $f^-$, $f^0$) were evaluated to identify the most likely reactive centers and to link key electronic descriptors with the degradation routes observed experimentally.

## 3. Results and discussions

### 3.1. *Structural and morphological properties*

The crystallographic structures of the pristine $CeVO_4$, $Bi_2Sn_2O_7$, and the 30 wt% $CeVO_4/Bi_2Sn_2O_7$ composite were examined using powder X-ray diffraction, and the corresponding diffraction patterns are presented in Fig. 1. The characteristic reflections of pure $CeVO_4$ appear at $2\theta =$ 18.9°, 28.9°, 30.1°, 34.3°, 47.4°, 50.2°, 53.4°, 56.5°, and 58.8°, which can be indexed to the (101), (112), (200), (004), (220), (204), (116), (312), and (224) crystal planes, respectively. These diffraction peaks are consistent with the tetragonal zircon-type $CeVO_4$ phase (JCPDS No. 01–079-1065), confirming the formation of a well-crystallized structure [43,44]. The XRD pattern of pristine $Bi_2Sn_2O_7$ exhibits distinct reflections at $2\theta$ values of 28.9°, 33.3°, 47.2°, 56.1°, and 59.5°. These peaks can be indexed to the (222), (400), (440), (622), and (444) planes, respectively, matching well with the reported cubic pyrochlore phase of $Bi_2Sn_2O_7$ (JCPDS No. 01–087-0284) [45]. The sharp and intense reflections indicate high crystallinity and phase purity of the $Bi_2Sn_2O_7$ nanoparticles synthesized through the hydrothermal route. In the case of the 30 wt% $CeVO_4/Bi_2Sn_2O_7$ composite, all major diffraction peaks associated with both $CeVO_4$ and $Bi_2Sn_2O_7$ phases are retained, and no additional reflections corresponding to impurities or secondary phases are observed, demonstrating the successful formation of a binary heterojunction without structural distortion. The coexistence of the $CeVO_4$ (112), (200), and (220) planes with the $Bi_2Sn_2O_7$ (222) and (400) planes clearly confirms the integration of both semiconductors. Notably, the relative intensity of the $CeVO_4$ peaks slightly decreases and broadens in the composite pattern, which can be attributed to the strong interfacial coupling between the two phases and partial lattice strain generated during hydrothermal assembly. Such microstructural modification is often associated with a reduction in coherent domain size and enhanced defect concentration, both of which can favor charge separation and light absorption in photocatalytic systems.

The $CeVO_4$ sample (Fig. 1b) exhibits aggregated microspheres composed of irregularly shaped nanoparticles with rough surfaces, indicative of self-assembled growth during hydrothermal synthesis. These clusters display an average particle size of approximately 200–300 nm, providing a relatively high surface roughness that favors light scattering and photon capture. In contrast, the $Bi_2Sn_2O_7$ nanoparticles (Fig. 1c) demonstrate a more compact, nearly spherical morphology with smoother surfaces and particle diameters in the range of 100–200 nm, consistent with the crystalline pyrochlore structure observed in the XRD pattern [46]. After compositing, the 30 wt% $CeVO_4/Bi_2Sn_2O_7$ heterojunction (Fig. 1d) shows a distinct morphological transformation in which fine $CeVO_4$ nanoparticles are uniformly anchored on the surface of the $Bi_2Sn_2O_7$ matrix. The red-boxed regions highlight these nanosized $CeVO_4$ domains intimately distributed across the $Bi_2Sn_2O_7$ framework, while the yellow-circled zones emphasize the preservation of the spherical $Bi_2Sn_2O_7$ cores. Such tight interfacial contact between the two semiconductors provides abundant active junctions that can facilitate efficient charge transfer across the $CeVO_4/Bi_2Sn_2O_7$ boundary under visible-light excitation. The hierarchical microstructure also helps to suppress particle agglomeration and increase the number of accessible reactive sites for photocatalytic reactions.

Further structural verification was obtained from the TEM micrograph of the composite (Fig. 1e), which clearly reveals the coexistence of darker $CeVO_4$ and lighter $Bi_2Sn_2O_7$ domains. The intimate interface between these two regions confirms the successful coupling of the tetragonal $CeVO_4$ and cubic $Bi_2Sn_2O_7$ phases, consistent with the XRD findings. The absence of discrete particle boundaries and the presence of a coherent contact zone suggest strong electronic interaction and lattice compatibility between the two semiconductors. Such a nanoscale configuration is expected to enhance interfacial charge migration, reduce electron–hole recombination, and consequently improve the overall photocatalytic efficiency [47].

The textural characteristics of $CeVO_4$, $Bi_2Sn_2O_7$, and the $CeVO_4/Bi_2Sn_2O_7$ composites were investigated through $N_2$ adsorption–desorption measurements, and the corresponding isotherms and pore-size distributions are presented in Fig. 1**(f–g)**. All samples display type IV isotherms with distinct $H_3$ hysteresis loops, characteristic of mesoporous materials formed by the aggregation of nanosized particles. The gradual increase in the adsorption volume with relative pressure indicates the prevalence of open mesopores, which facilitate molecular diffusion and adsorption processes during photocatalysis. As summarized in **Table S1**, the BET surface area of pure $CeVO_4$ (67.3 m$^2$ g$^{-1}$) is considerably lower than that of $Bi_2Sn_2O_7$ (99.6 m$^2$ g$^{-1}$) owing to its denser particle agglomeration. Upon formation of the heterojunction, the surface area markedly increases with $CeVO_4$ incorporation, reaching a maximum value of 137.1 m$^2$ g$^{-1}$ for the 30 wt% $CeVO_4/Bi_2Sn_2O_7$ composite. This enhancement arises from the uniform distribution of finely dispersed $CeVO_4$ nanocrystals over the $Bi_2Sn_2O_7$ matrix, which inhibits aggregation and introduces additional mesoporous channels at the interfaces. Further loading of $CeVO_4$ to 40 wt% leads to a minor decline in surface area (131.0 m$^2$ g$^{-1}$), attributable to partial pore blockage by excess $CeVO_4$ nanoparticles [48]. The BJH pore-size distribution curves (Fig. 1g) reveal mesoporous frameworks with mean pore diameters between 32 and 43 nm. The composite samples exhibit broader and slightly shifted pore distributions toward larger diameters compared to the pristine oxides, reflecting the creation of interparticle voids and hierarchical pores during heterojunction assembly. Moreover, the total pore volume rises from 0.20 cm$^3$ g$^{-1}$ for $CeVO_4$ to 0.40 cm$^3$ g$^{-1}$ for the 30 wt% composite, further confirming improved textural accessibility and enhanced porosity. These structural enhancements—higher surface area, enlarged pore volume, and hierarchical mesoporosity play a pivotal role in boosting photocatalytic efficiency.

XPS was employed to elucidate the surface composition and interfacial electronic structure of the $CeVO_4/Bi_2Sn_2O_7$ heterostructure (Fig. 1h–m)**.** To further demonstrate that the coupled material is a true heterojunction (electronic coupling at an interface) rather than a simple physical mixture, the high-resolution spectra of the composite were compared with those of the pristine components (**Fig. S1a–e**). In this comparative analysis, the key evidence is not only the preservation of the expected oxidation states ($Ce^{3+}/Ce^{4+}$, $V^{5+}$, $Bi^{3+}$, $Sn^{4+}$) but also the systematic binding-energy shifts that occur after coupling, which reflect interfacial charge redistribution and band bending. The wide-scan XPS spectrum verifies the presence of Ce, V, Bi, Sn, and O, confirming effective integration of the two oxide components and indicating that no measurable extraneous elements are present on the catalyst surface. For Ce 3d, pristine $CeVO_4$ (**Fig. S1a**) shows the characteristic multiple envelopes of mixed-valence cerium, containing resolvable components assigned to $Ce^{3+}$ and $Ce^{4+}$. The composite (Fig. 1i) retains these $Ce^{3+}/Ce^{4+}$ features, indicating that the $CeVO_4$ lattice chemistry is preserved after hybridization. The coexistence of $Ce^{3+}$ and $Ce^{4+}$ is also chemically meaningful because it implies a redox-flexible cerium environment that is frequently associated with oxygen-vacancy-related defect chemistry and reversible surface electron storage. Such mixed valence can facilitate interfacial charge regulation by transiently trapping/delocalizing electrons, thereby suppressing electron–hole recombination during photocatalysis. Importantly, any subtle shift of the Ce 3d envelope after coupling (relative to pristine $CeVO_4$) is consistent with interfacial electronic interaction rather than a mere superposition of two independent spectra [49]. The simultaneous presence of $Ce^{3+}$ and $Ce^{4+}$ species demonstrates a mixed-valence state within the $CeVO_4$ lattice, indicative of abundant oxygen vacancies and defect sites. These $Ce^{3+}/Ce^{4+}$ redox pairs can act as efficient electron reservoirs, promoting dynamic charge transfer across the heterojunction interface and thus suppressing electron–hole recombination during photocatalysis [50]. This mixed-valence feature is chemically meaningful because it indicates a redox-flexible cerium environment that is often coupled with defect chemistry (e.g., oxygen-vacancy-associated $Ce^{3+}$ formation) and can facilitate interfacial charge regulation under irradiation. The V 2p spectrum provides a clear indicator of electronic interaction on the $CeVO_4$ side. In pristine $CeVO_4$ (**Fig. S1b**), the V 2p doublet is centered at 517.21 eV (V $2p_{3/2}$) and 524.28 eV (V $2p_{1/2}$), consistent with $V^{5+}$ in $VO_4^{3-}$ units. After coupling, the corresponding peaks in the composite (Fig. 1j) appear at 517.09 eV and 524.11 eV, showing a negative shift relative to the pristine material. A shift toward lower binding energy indicates increased electron density around vanadium sites, supporting electron enrichment on the $CeVO_4$ side induced by interfacial contact [51]. The O 1 s spectra further reinforce the heterojunction interpretation by reflecting both lattice oxygen and defect-related surface chemistry. Pristine $Bi_2Sn_2O_7$ (**Fig. S1c**) can be deconvoluted into lattice oxygen at 529.42 eV, a defect/vacancy-related component at 531.25 eV, and surface-adsorbed oxygen at ~532.31 eV. The composite O 1 s spectrum (Fig. 1k) similarly contains lattice oxygen and a pronounced defect-associated contribution near ~531.25 eV, together with a higher-binding-energy adsorbed-oxygen component. The persistence and prominence of the defect-related oxygen signal indicate an oxygen-vacancy-involved surface, which can enhance carrier transport, promote adsorption/activation of $O_2$/$CO_2$, and facilitate reactive oxygen species generation. Therefore, the O 1 s results provide functional evidence that complements the binding-energy shift analysis [52]. These vacancies not only enhance charge carrier mobility but also facilitate the adsorption and activation of molecular oxygen, thereby accelerating the generation of reactive oxygen species during photocatalytic reactions. On the $Bi_2Sn_2O_7$ side, pristine $Bi_2Sn_2O_7$ (**Fig. S1d**) exhibits Bi 4f peaks at 158.88 eV (Bi $4f_{7/2}$) and 164.09 eV (Bi $4f_{5/2}$), characteristic of $Bi^{3+}$. In the composite (Fig. 1l), the Bi 4f doublet is maintained (confirming the preservation of the $Bi_2Sn_2O_7$ framework) but shifts slightly to higher binding energy (e.g., 158.91/164.18 eV). This positive shift suggests reduced electron density at Bi sites after coupling, consistent with electron transfer away from $Bi_2Sn_2O_7$ during heterojunction formation [53]. Similarly, the Sn core levels support this trend. Pristine $Bi_2Sn_2O_7$ (**Fig. S1e**) shows the Sn 3d doublet at 485.91 eV (Sn $3d_{5/2}$) and 494.36 eV (Sn $3d_{3/2}$), indicative of $Sn^{4+}$ in the pyrochlore lattice. In the composite (Fig. 1m), these peaks shift to higher binding energies (e.g., 486.26/494.72 eV), again pointing to electron depletion around Sn sites upon heterojunction formation. The concurrent positive shifts of Bi 4f and Sn 3d, together with the negative shift of V 2p, provide a consistent picture of interfacial charge redistribution rather than a physical mixture of two electronically isolated phases [54]. Overall, comparing the pristine XPS spectra (Fig. S1a–e) with those of the composite (Fig. 1h–m) demonstrates that the expected oxidation states of all constituent elements are preserved ($Ce^{3+}/Ce^{4+}$, $V^{5+}$, $Bi^{3+}$ and $Sn^{4+}$), confirming that the heterostructure is not formed by decomposition into unintended phases. More importantly, the systematic and directionally consistent binding-energy shifts (V 2p toward lower binding energy, whereas Bi 4f and Sn 3d shift toward higher binding energy) provide compelling evidence of interfacial electron redistribution and the establishment of a built-in electric field, which are defining signatures of a true heterojunction rather than a simple physical mixture. Collectively, the XPS results verify that the $CeVO_4/Bi_2Sn_2O_7$ composite comprises mixed-valence $Ce^{3+}/Ce^{4+}$, $V^{5+}$, $Bi^{3+}$, $Sn^{4+}$, and multiple oxygen species, and that the pronounced defect-related O 1 s contribution reflects an oxygen-vacancy-rich surface. These vacancies offer functional implications beyond elemental-state assignment by improving charge transport, strengthening surface adsorption/activation of reactants, and facilitating reactive oxygen species generation, thereby accelerating SMX oxidation and promoting more efficient utilization of photogenerated electrons for $CO_2$ conversion. Overall, the XPS evidence supports that the enhanced dual-function activity arises from heterointerface-enabled charge redistribution coupled with defect-assisted surface reaction kinetics, rather than from secondary-phase formation or unstable cation valence changes.

### 3.2. *Photocatalytic activity toward SMX degradation*

The photocatalytic degradation efficiency of SMX under visible-light irradiation over the synthesized photocatalysts is presented in Fig. 1n. The blank test (without catalyst) exhibited negligible SMX removal (4.58%), indicating that self-photolysis of the pollutant is insignificant under the experimental conditions. In contrast, pure $CeVO_4$ and $Bi_2Sn_2O_7$ achieved degradation efficiencies of 24.86% and 38.21%, respectively, after the same irradiation period. The modest activity of $CeVO_4$ can be attributed to its narrow band gap but poor charge-carrier separation, while $Bi_2Sn_2O_7$, despite its broader light-absorption window, suffers from limited redox potential and rapid electron–hole recombination. Upon coupling $CeVO_4$ with $Bi_2Sn_2O_7$, a remarkable enhancement in photocatalytic performance was observed. The degradation efficiencies increased progressively with $CeVO_4$ loading, reaching 50.29%, 58.76%, and 73.57% for the 10%, 20%, and 30 wt% $CeVO_4/Bi_2Sn_2O_7$ composites, respectively. The adsorption capacities also followed a similar upward trend, confirming that the heterojunction structure provides an expanded surface area and abundant accessible active sites for pollutant capture and reaction [55]. The photocatalytic activity reached its optimum for the 30 wt% $CeVO_4/Bi_2Sn_2O_7$ sample, achieving an impressive 88.42% SMX degradation, which is more than twice that of pristine $Bi_2Sn_2O_7$ and over three times higher than $CeVO_4$ alone [56].

The superior performance of the 30 wt% composite can be attributed to several synergistic factors. First, at this loading, $CeVO_4$ nanoparticles are uniformly distributed over the $Bi_2Sn_2O_7$ surface, forming intimate interfacial contact that facilitates efficient charge separation through a *Z*-scheme electron-transfer pathway. This architecture allows photogenerated electrons in $CeVO_4$ and holes in $Bi_2Sn_2O_7$ to participate simultaneously in redox reactions while suppressing carrier recombination. Second, the optimized $CeVO_4$ content introduces a high density of oxygen vacancies and $Ce^{3+}/Ce^{4+}$ redox couples, which serve as shallow traps and promote rapid interfacial charge migration. Third, the increased BET surface area and mesoporous texture (as confirmed by nitrogen adsorption analysis) improve light absorption, molecular diffusion, and the accessibility of active sites. When the $CeVO_4$ content was further increased to 40 wt%, the degradation efficiency slightly declined to 82.9%. This reduction can be ascribed to partial surface shielding and particle agglomeration at higher $CeVO_4$ loadings, which hinder photon penetration and limit active-site exposure [57]. Therefore, the 30 wt% $CeVO_4/Bi_2Sn_2O_7$ composite represents an optimal structural and electronic configuration that maximizes light harvesting, charge separation, and reactive-species generation, resulting in its outstanding photocatalytic activity toward SMX degradation.

### 3.3. Effect of operational parameters on the SMX degradation

The photocatalytic degradation performance of SMX is significantly influenced by various operational parameters, including pH, catalyst dosage, initial pollutant concentration, and reaction time. The interplay between these parameters governs the adsorption capacity, surface charge interactions, and overall efficiency of photocatalytic oxidation. The surface charge characteristics of the optimized 30 wt% $CeVO_4/Bi_2Sn_2O_7$ composite, determined via zeta potential analysis, are shown in Fig. 2a. The point of zero charge ($pH_{PZC}$) is observed at 4.93, indicating that the catalyst surface is positively charged at $pH < 4.93$ and negatively charged at $pH > 4.93$. Meanwhile, as illustrated in Fig. 2b, SMX exists as a cation ($SMX^+$) below its first dissociation constant ($pKa_1 = 1.88$), as a zwitterion ($SMX^0$) between $pKa_1 = 1.88$ and $pKa_2 = 5.6$, and predominantly in an anionic form ($SMX^-$) above $pKa_2 = 5.6$. Therefore, the adsorption affinity between the SMX molecules and catalyst surface varies with pH due to electrostatic interactions between the charged species [58].

The influence of catalyst dosage on the photocatalytic degradation of SMX using the 30 wt% $CeVO_4/Bi_2Sn_2O_7$ composite was systematically evaluated in the range of 0.10–0.25 g $L^{-1}$, and the corresponding degradation efficiencies after 70 min of visible-light irradiation are presented in Fig. 2c. The degradation performance exhibited a pronounced enhancement with increasing catalyst dosage, rising from 74.9% at 0.10 g $L^{-1}$ to 98.34% at 0.25 g $L^{-1}$. At low catalyst loading (0.10 g $L^{-1}$), the relatively small number of photocatalyst particles provides limited surface-active sites and light absorption area, resulting in the generation of an insufficient quantity of photogenerated radicals ($\bullet O_2^-$ and $\bullet OH$) to completely oxidize the SMX molecules. As the dosage increases to 0.15 g $L^{-1}$, the degradation efficiency improves markedly to 86.3%, which can be attributed to the larger specific surface area and greater number of heterojunction interfaces available for redox reactions. A further increase to 0.20 g $L^{-1}$ results in 93.6% degradation efficiency, indicating that a higher particle concentration effectively enhances photon utilization and charge-carrier separation due to the intimate interfacial contact between $CeVO_4$ and $Bi_2Sn_2O_7$ components [59]. The maximum degradation efficiency of 98.34% was obtained at 0.25 g $L^{-1}$, beyond which no significant improvement is expected. At this optimal dosage, sufficient light absorption and surface accessibility are achieved without inducing excessive scattering or aggregation. The abundant heterojunction sites promote rapid transfer of photogenerated electrons from the conduction band of $CeVO_4$ to that of $Bi_2Sn_2O_7$, while holes migrate in the opposite direction, effectively suppressing electron–hole recombination. Consequently, a larger population of reactive oxygen species is produced, accelerating SMX oxidation and mineralization [60].

The influence of initial SMX concentration on the photocatalytic performance of the 30 wt% $CeVO_4/Bi_2Sn_2O_7$ composite was

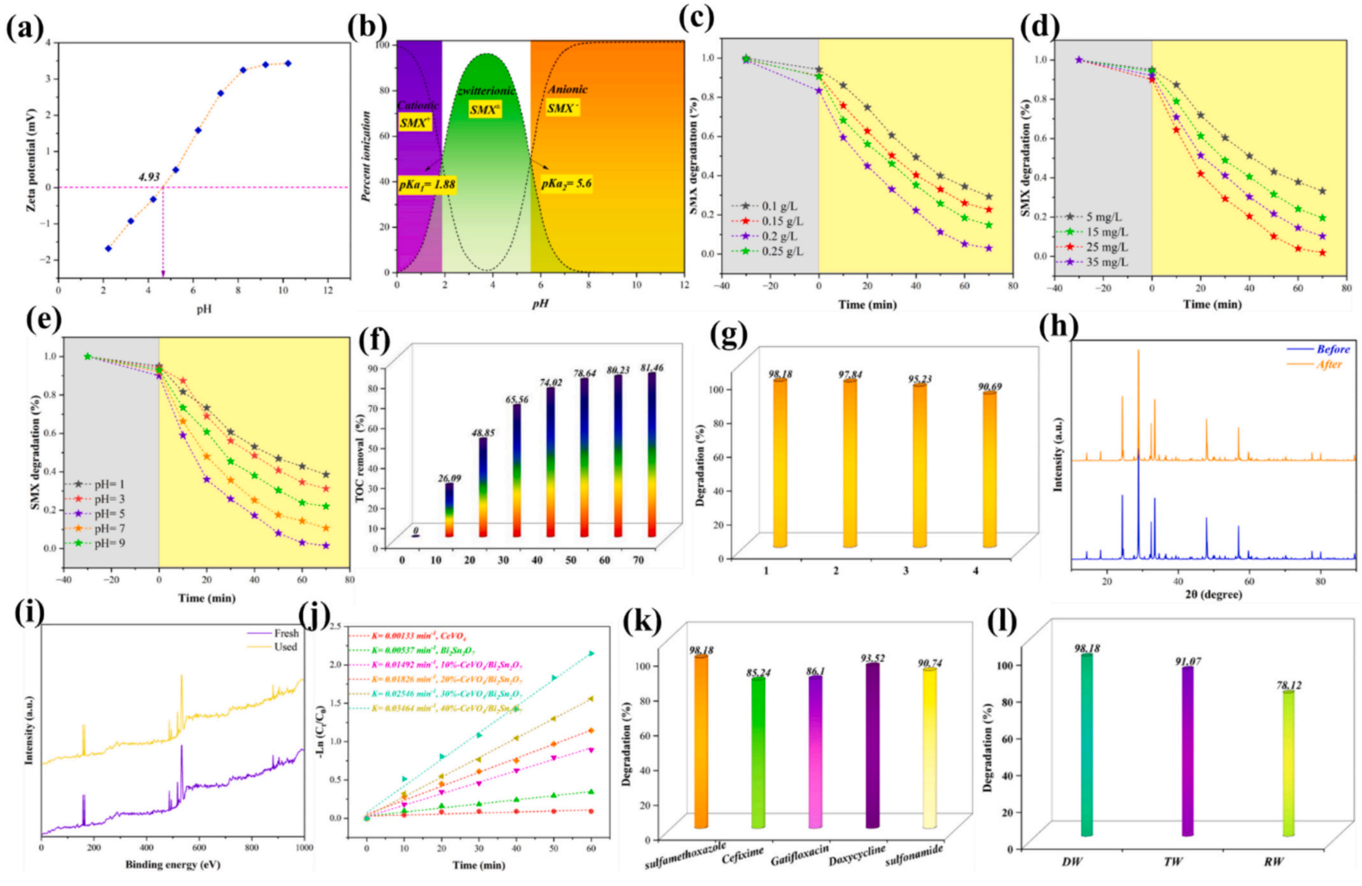

**Fig. 2.** Effect of operational parameters on SMX degradation using the 30 wt% $CeVO_4/Bi_2Sn_2O_7$ photocatalyst: (a–b) pH and ionization behavior, (c–e) influence of dosage, concentration, and pH, (f) TOC removal, (g–i) stability evaluation by cycling, XRD, and XPS, (j) kinetic fitting, and (k–l) degradation performance toward various antibiotics and in different water matrices.

systematically investigated within the range of 5–35 mg $L^{-1}$, as depicted in Fig. 2d. The degradation efficiency after 70 min of visible-light irradiation exhibited a strong dependence on pollutant concentration, reaching 98.1% at 25 mg $L^{-1}$, while lower and higher concentrations resulted in slightly reduced efficiencies of 88.7% (5 mg $L^{-1}$), 93.4% (15 mg $L^{-1}$), and 84.9% (35 mg $L^{-1}$), respectively. At lower initial concentrations (5–15 mg $L^{-1}$), the total number of SMX molecules in the solution is relatively small compared with the available photoactive sites and photogenerated radicals ($\bullet O_2^-$ and •OH). Consequently, only a limited portion of the incident photons is utilized for pollutant oxidation, leading to moderate degradation efficiencies. As the concentration increases to 25 mg $L^{-1}$, the number of SMX molecules becomes sufficient to interact effectively with the generated radicals, ensuring efficient utilization of photoexcited charge carriers and maximizing visible-light absorption. Under this condition, the system achieves an optimal balance between radical generation, molecular adsorption, and interfacial charge transfer across the $CeVO_4/Bi_2Sn_2O_7$ heterojunction, resulting in the highest degradation efficiency of nearly 98%. However, when the concentration is further increased to 35 mg $L^{-1}$, a noticeable decrease in photocatalytic activity occurs. This decline can be attributed to several concurrent effects: (i) excessive SMX molecules compete for a finite number of active sites, leading to surface saturation; (ii) the solution becomes optically dense, attenuating light penetration (inner-filter effect); and (iii) intermediate by-products generated during partial oxidation competitively adsorb on the catalyst surface, hindering further reaction. These factors collectively reduce the availability of reactive radicals and suppress the overall degradation rate [61].

The influence of the initial solution pH on the photocatalytic degradation of SMX over the 30 wt% $CeVO_4/Bi_2Sn_2O_7$ composite was evaluated in the pH range of 1–9, and the corresponding degradation efficiencies after 70 min of visible-light irradiation are presented in Fig. 2e. The results reveal a clear pH-dependent trend, with the degradation efficiency initially increasing from 72.3% at pH 1 to a maximum of 98.0% at pH 5, followed by a decline to 89.4% and 76.7% at pH 7 and 9, respectively. This strong correlation between pH and photocatalytic performance arises from the interplay between the surface charge of the catalyst and the speciation of SMX molecules in aqueous solution. As shown previously (Fig. 2a–b), the 30 wt% $CeVO_4/Bi_2Sn_2O_7$ composite has a point of zero charge ($pH_{pzc}$) of 4.93, meaning that its surface is positively charged in acidic media (pH < 4.93) and negatively charged in alkaline media (pH > 4.93). Meanwhile, SMX exists in cationic form ($SMX^+$) below $pKa_1 = 1.88$, in zwitterionic form ($SMX^0$) between $pKa_1 = 1.88$ and $pKa_2 = 5.6$, and predominantly as an anion ($SMX^-$) above $pKa_2 = 5.6$. At pH = 5, the surface charge of the photocatalyst is close to neutral while SMX primarily exists in its zwitterionic form. This condition minimizes electrostatic repulsion and promotes strong molecular adsorption through dipole–dipole and hydrogen-bonding interactions, leading to optimal contact between SMX molecules and photoactive sites [62]. As a result, charge transfer across the $CeVO_4/Bi_2Sn_2O_7$ interface and the generation of reactive oxygen species ($\bullet O_2^-$ and •OH) are significantly enhanced, resulting in near-complete SMX degradation (~98%). In strongly acidic environments (pH 1–3), both the catalyst surface and SMX molecules carry positive charges, resulting in electrostatic repulsion that reduces adsorption efficiency and hinders electron–hole transfer. Conversely, at alkaline pH values (≥ 7), the catalyst surface becomes negatively charged while SMX is predominantly anionic ($SMX^-$), again causing repulsive interactions and limiting adsorption. Additionally, under basic conditions, excessive hydroxyl ions may act as scavengers for photogenerated holes, lowering •OH radical production and thereby decreasing degradation efficiency.

### 3.4. TOC removal, stability, reusability, and durability of the Photocatalyst

The photocatalytic mineralization efficiency of the optimized 30 wt % $CeVO_4/Bi_2Sn_2O_7$ composite was assessed through total organic carbon (TOC) analysis and recycling experiments to confirm its practical applicability and stability during repeated operation. As illustrated in Fig. 2f, the TOC removal progressively increased with irradiation time, achieving 26.09%, 48.85%, 65.56%, 74.02%, 78.64%, 80.23%, and 81.46% after 10, 20, 30, 40, 50, 60 and 70 min, respectively. This gradual enhancement in mineralization efficiency signifies the effective oxidation of SMX and its intermediates into simple inorganic species such as $CO_2$, $H_2O$, $NO_3^-$, and $SO_4^{2-}$. The observed high TOC removal after 60 min underscores the superior charge separation and reactive oxygen species (ROS) generation capabilities of the $CeVO_4/Bi_2Sn_2O_7$ heterostructure, ensuring deep oxidation rather than partial degradation of SMX molecules.

To further evaluate its reusability, the photocatalytic activity of the composite was tested for four consecutive cycles under identical conditions (Fig. 2g). The degradation efficiency decreased slightly from 98.18% in the first cycle to 97.84%, 95.23%, and 90.69% in the second, third, and fourth runs, respectively. The minor reduction in activity (< 8%) after four cycles can be attributed to partial surface fouling by residual intermediates or minor catalyst loss during recovery. However, the consistently high degradation efficiency demonstrates the excellent durability and structural integrity of the $CeVO_4/Bi_2Sn_2O_7$ heterojunction during prolonged operation. The crystalline and chemical stability of the photocatalyst before and after four consecutive degradation cycles were examined using XRD and XPS analyses. As depicted in Fig. 2h, the XRD diffraction peaks of the used catalyst remain nearly identical to those of the fresh one, with no detectable phase transformation, new impurity peaks, or intensity loss. The characteristic reflections of $CeVO_4$ and $Bi_2Sn_2O_7$ are clearly preserved, confirming that the heterojunction maintains its crystallinity and structural integrity even after multiple photocatalytic reactions [63]. Complementary XPS survey spectra (Fig. 2i) further validate the chemical stability of the composite. The elemental signals of Ce 3d, V 2p, Bi 4f, Sn 3d, and O 1 s are retained with negligible shifts in binding energy, indicating that the oxidation states of the constituent elements remain unchanged. The persistence of these spectral features confirms that the $CeVO_4/Bi_2Sn_2O_7$ heterointerface remains electronically and chemically stable throughout cyclic photocatalysis [64].

The reaction kinetics of SMX degradation over the as-prepared photocatalysts were analyzed using a pseudo-first-order kinetic model, expressed as $-\ln(C/C_0) = kt$, where k ($min^{-1}$) denotes the apparent rate constant and $C_0$ and C represent the initial and instantaneous SMX concentrations, respectively. The linear plots of $-\ln(C/C_0)$ versus irradiation time for different catalysts are presented in Fig. 2j, with the corresponding rate constants summarized in the inset. Among all the catalysts, the 30 wt% $CeVO_4/Bi_2Sn_2O_7$ composite exhibited the highest rate constant ($k = 0.02546\ min^{-1}$), markedly outperforming pure $CeVO_4$ ($k = 0.00133\ min^{-1}$) and $Bi_2Sn_2O_7$ ($k = 0.00537\ min^{-1}$). The rate constants for the other composites followed the order: 40% $CeVO_4/Bi_2Sn_2O_7$ ($0.03464\ min^{-1}$) > 30% ($0.02546\ min^{-1}$) > 20% ($0.01826\ min^{-1}$) > 10% ($0.01492\ min^{-1}$), confirming that the photocatalytic efficiency strongly depends on the $CeVO_4$ loading ratio. The incorporation of an optimal 30 wt% $CeVO_4$ onto $Bi_2Sn_2O_7$ creates a well-balanced heterojunction that facilitates efficient charge separation and visible-light utilization, while maintaining a high surface area and sufficient interfacial contact between both semiconductors. The poor kinetic performance of pristine $CeVO_4$ can be attributed to its rapid charge recombination and narrow light absorption range, whereas pure $Bi_2Sn_2O_7$ suffers from limited photoresponse and low conductivity. At low $CeVO_4$ content (10–20 wt%), insufficient junction formation restricts interfacial electron–hole migration, leading to lower k values. Conversely, excessive $CeVO_4$ loading (40 wt%) partially blocks the active sites of $Bi_2Sn_2O_7$ and induces light-shielding effects, which slightly reduce the accessible surface area and reactive species generation efficiency [65].

The photocatalytic versatility of the optimized 30 wt% $CeVO_4/Bi_2Sn_2O_7$ composite was further assessed by evaluating its degradation efficiency toward various antibiotic pollutants and in different water matrices. As depicted in Fig. 2k, the composite exhibited outstanding degradation efficiency across a range of representative antibiotics, including sulfamethoxazole (SMX, 98.18%), cefixime (85.24%), gatifloxacin (86.10%), doxycycline (93.52%), and sulfonamide (90.74%). Among these, SMX demonstrated the highest degradation efficiency, which can be attributed to its favorable adsorption affinity toward the catalyst surface and its high photoreactivity under visible-light irradiation. The strong π–π interactions between SMX's aromatic rings and the oxygen-rich surface of $CeVO_4/Bi_2Sn_2O_7$ enhance charge transfer and facilitate oxidative degradation. In contrast, cefixime and gatifloxacin exhibited slightly lower efficiencies due to their more complex molecular structures and multiple heterocyclic substituents that hinder reactive oxygen species (ROS) attack. Doxycycline and sulfonamide displayed intermediate efficiencies, suggesting that molecular charge distribution, functional groups, and steric hindrance collectively govern photocatalytic degradation behavior.

To examine the catalyst's environmental applicability, degradation experiments were also conducted in different water matrices—deionized water (DW), tap water (TW), and real wastewater (RW)—as shown in Fig. 2l. The photocatalytic efficiency followed the order: DW (98.18%) > TW (91.07%) > RW (78.12%). The high efficiency in deionized water arises from the absence of interfering ions and organic impurities, allowing maximum photon absorption and reactive species generation. In tap water, the presence of common inorganic ions, partially scavenges hydroxyl radicals (•OH) and superoxide radicals (•$O_2^-$), thereby reducing degradation efficiency. The lowest performance in real wastewater can be attributed to the coexistence of competing organic and inorganic constituents, turbidity, and ionic species that quench ROS or block the active surface sites of the catalyst.

### 3.5. Detection of degradation pathways of SMX and toxicity evaluation

To elucidate the degradation mechanism of SMX over the 30 wt% $CeVO_4/Bi_2Sn_2O_7$ heterojunction, liquid chromatography–mass spectrometry (LC–MS) analysis was conducted to identify intermediate byproducts (**Fig. S3**). Based on the detected ions and previous literature reports, four plausible degradation pathways (I–IV) were proposed, as

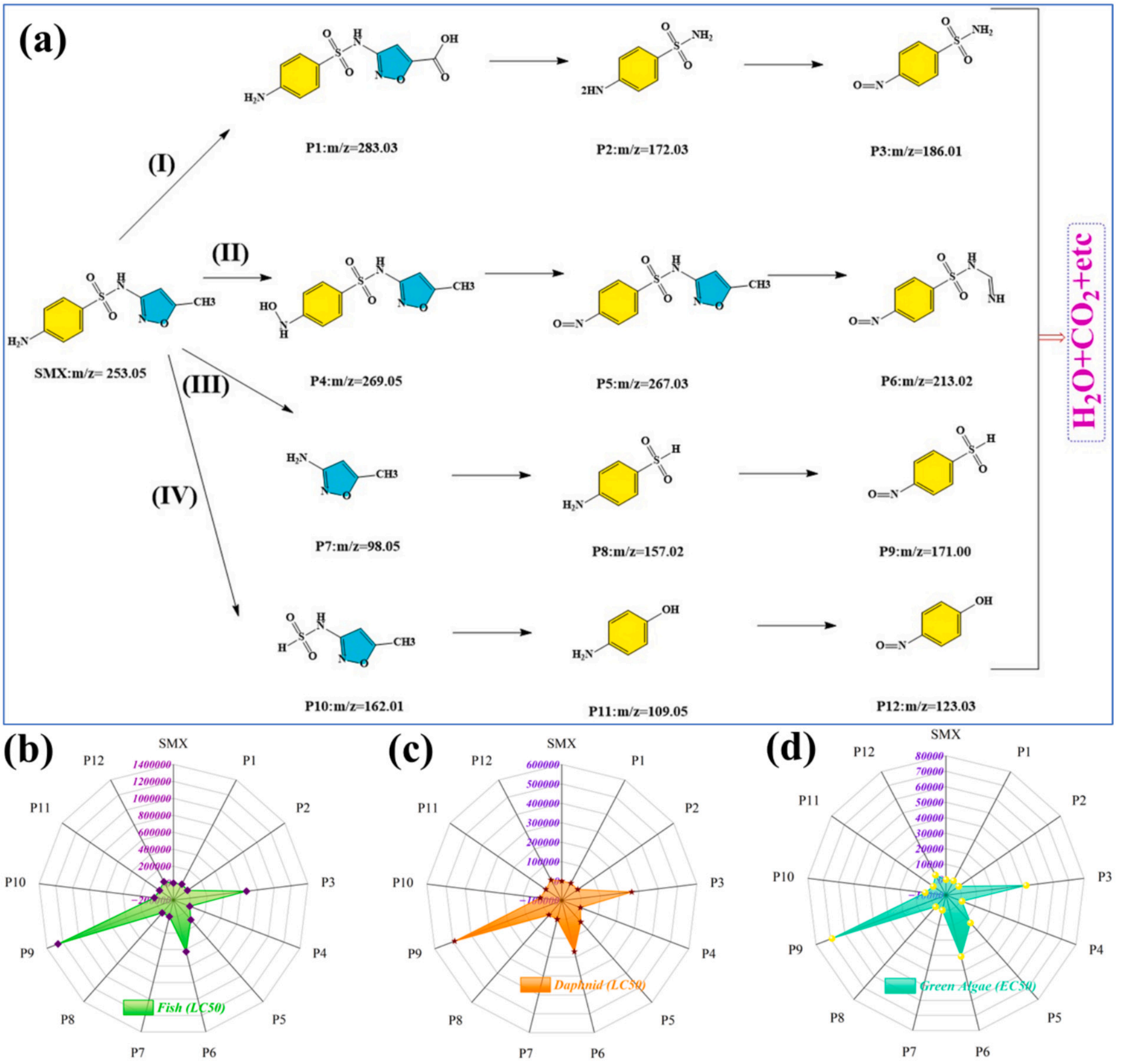

**Fig. 3.** (a) Proposed photocatalytic degradation pathways of SMX over 30 wt% $CeVO_4/Bi_2Sn_2O_7$ derived from LC–MS analysis, and (b–d) predicted toxicity of SMX and its intermediates toward fish, daphnid, and green algae, showing a marked reduction in ecological risk after degradation. (For interpretation of the references to color in this figure legend, the reader is referred to the web version of this article.)

illustrated in Fig. 3a. In Pathway I, SMX (*m/z* = 253.05) undergoes hydroxyl radical (•OH)-induced oxidation at the methyl site of the isoxazole ring, generating P1 (m/z = 283.03). Subsequent cleavage of the isoxazole moiety leads to the formation of P2 (m/z = 172.03), which then experiences amino-group oxidation to yield P3 (m/z = 186.01). In Pathway II, the reaction initiates with the oxidation of the amine group to form hydroxylated intermediate P4 (m/z = 269.05). P4 further undergoes nitro-substitution and ring-opening processes, giving rise to P5 (m/z = 267.03) and P6 (m/z = 213.02), respectively [66]. Pathway III involves N—S bond cleavage of the sulfonamide linkage, resulting in the generation of P7 (m/z = 98.05) and P8 (m/z = 157.02) [67]. P8 then undergoes oxidation of the amino functionality, producing P9 (m/z = 171.00). In Pathway IV, C—S bond scission occurs, producing intermediates P10 (m/z = 162.01) and P11 (m/z = 109.05). Further

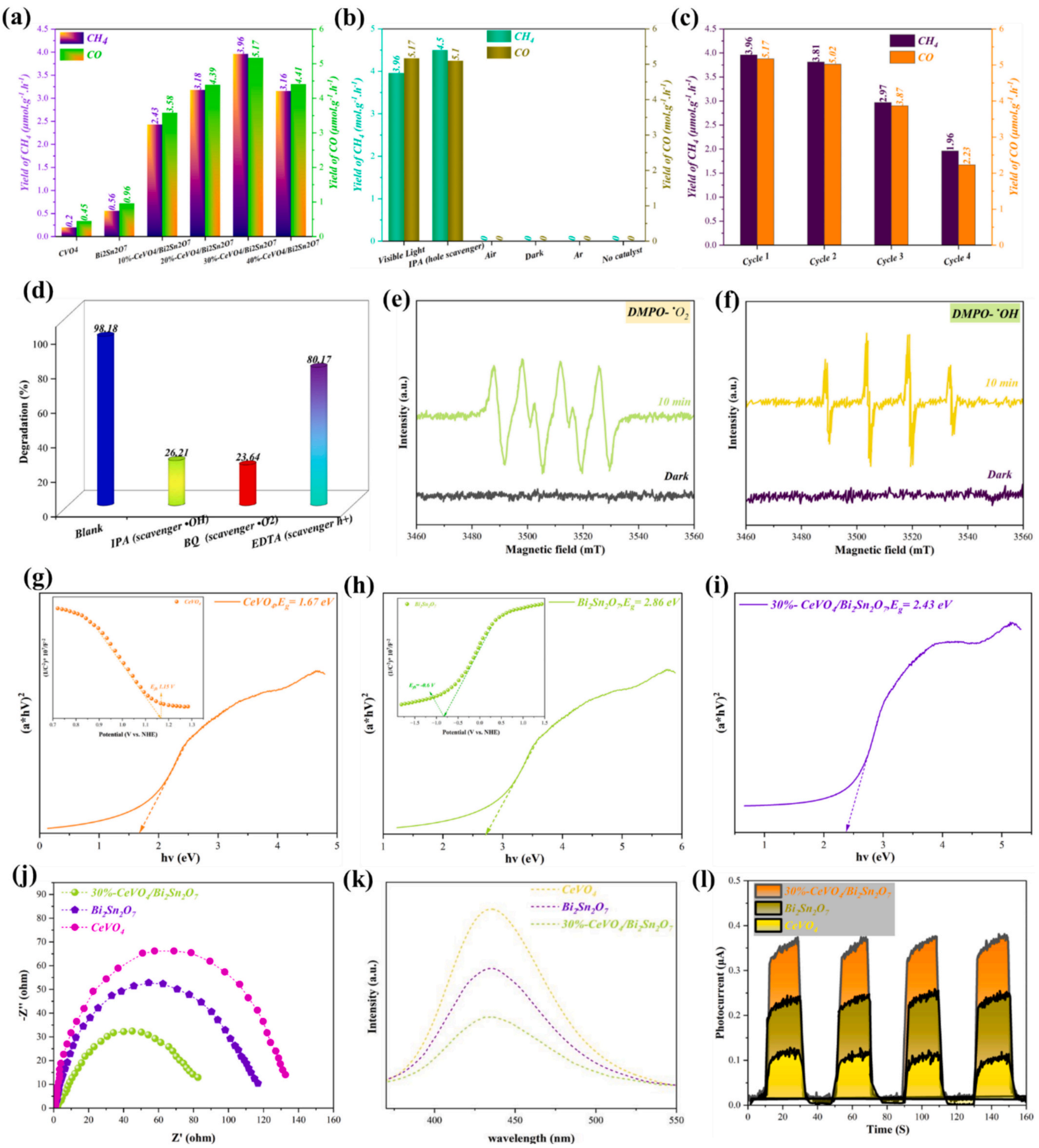

**Fig. 4.** (a–c) Photocatalytic $CO_2$ reduction activity, control tests, and recyclability of $CeVO_4/Bi_2Sn_2O_7$ composites; (d–f) Reactive species trapping and ESR spectra confirming •OH and $•O_2^-$ generation; (g–i) UV–Vis DRS and Mott–Schottky plots showing band structures of $CeVO_4$, $Bi_2Sn_2O_7$, and 30 wt% $CeVO_4/Bi_2Sn_2O_7$; (j–l) EIS, PL, and photocurrent results verifying enhanced charge separation and transfer in the 30 wt% $CeVO_4/Bi_2Sn_2O_7$ heterojunction.

oxidation of the amine group and hydroxylation reactions result in the formation of P12 (m/z = 123.03) [10]. Ultimately, these intermediates are continuously attacked by reactive oxygen species (•OH and $•O_2^-$), leading to progressive demethylation, desulfonation, and ring-opening reactions. The complete mineralization of SMX proceeds through oxidation to innocuous end-products such as $CO_2$, $H_2O$, and inorganic ions ($NO_3^-$, $SO_4^{2-}$). These findings confirm that the $CeVO_4/Bi_2Sn_2O_7$ heterojunction effectively promotes multistep degradation via combined oxidation and cleavage processes under visible-light irradiation (See Fig. 4).

Given the detection of multiple SMX degradation intermediates, it is crucial to assess their potential ecological toxicity. The acute and chronic toxicities of SMX and its degradation products were evaluated toward three representative aquatic organisms—fish, daphnid, and green algae—using the ECOSAR predictive model under the framework of the Globally Harmonized System (GHS) classification. The semi-lethal concentration ($LC_{50}$), semi-effective concentration ($EC_{50}$), and chronic toxicity value (ChV) were employed as toxicity indicators. As shown in Figs. 3b–3d, the majority of detected intermediates (P1–P12) exhibit significantly reduced toxicity levels compared to the parent SMX molecule. This notable decrease can be attributed to the disruption of the aromatic sulfonamide structure and the oxidative cleavage of N—S and C—S bonds, which substantially diminish bioactivity and environmental persistence. Among all intermediates, P7, P8, and P11 retained moderate toxicity levels comparable to SMX due to the presence of aromatic or amino-sulfonyl groups that can still interact with biological receptors. Nevertheless, their transient nature and further degradation into less harmful species mitigate long-term ecological risk. Collectively, these results indicate that the photocatalytic degradation process not only effectively decomposes SMX but also transforms toxic pharmaceutical residues into low-toxicity or environmentally benign compounds.

### 3.6. Photocatalytic $CO_2$ conversion

The photocatalytic reduction of $CO_2$ was carried out under visible-light irradiation to evaluate the dual-functional performance of the synthesized photocatalysts, and the corresponding results are presented in **Figs. 4a–4c**. As shown in **Fig. 4a**, both $CH_4$ and CO were generated as the main carbon-containing products for all tested samples, confirming the efficient photo-reduction of $CO_2$ over the $CeVO_4/Bi_2Sn_2O_7$ composites. Quantitatively, pristine $CeVO_4$ and $Bi_2Sn_2O_7$ exhibited very limited activities, producing only 0.20 μmol $g^{-1}$ $h^{-1}$ of $CH_4$ and 0.45 μmol $g^{-1}$ $h^{-1}$ of CO for $CeVO_4$, and 0.56 μmol $g^{-1}$ $h^{-1}$ of $CH_4$ and 0.96 μmol $g^{-1}$ $h^{-1}$ of CO for $Bi_2Sn_2O_7$. Upon coupling $CeVO_4$ with $Bi_2Sn_2O_7$, the photocatalytic efficiency increased dramatically, confirming that heterojunction formation effectively enhances charge separation and $CO_2$ activation [68]. The 10%, 20%, 30%, and 40% $CeVO_4/Bi_2Sn_2O_7$ composites yielded 2.43, 3.18, 3.96, and 3.16 μmol $g^{-1}$ $h^{-1}$ of $CH_4$, respectively, and 3.58, 4.39, 5.17, and 4.41 μmol $g^{-1}$ $h^{-1}$ of CO, respectively. Notably, the 30 wt% $CeVO_4/Bi_2Sn_2O_7$ exhibited the highest product yields—3.96 μmol $g^{-1}$ $h^{-1}$ ($CH_4$) and 5.17 μmol $g^{-1}$ $h^{-1}$ (CO)—demonstrating its optimal interfacial configuration and superior photoactivity [69]. This enhanced yield corresponds to a 19.8-fold ($CH_4$) and 11.5-fold (CO) increase compared with pure $CeVO_4$, and a 7.1-fold ($CH_4$) and 5.4-fold (CO) improvement relative to $Bi_2Sn_2O_7$, evidencing the decisive synergistic effect of the heterojunction [70]. The remarkable $CO_2$ reduction efficiency of the 30 wt% $CeVO_4/Bi_2Sn_2O_7$ heterojunction arises from several synergistic mechanisms. First, the *Z*-scheme charge transfer pathway between $CeVO_4$ and $Bi_2Sn_2O_7$ maintains the strong redox potentials of each component, as the photogenerated electrons in the CB of $CeVO_4$ ($E_{CB} = 1.25$ eV) and the holes in the VB of $Bi_2Sn_2O_7$ ($E_{VB} = 2.16$ eV) remain highly active. This configuration facilitates spatial charge migration and suppresses recombination, thereby enhancing both reduction and oxidation half-reactions. Second, the presence of $Ce^{3+}/Ce^{4+}$ and $V^{4+}/V^{5+}$ redox pairs in $CeVO_4$ creates efficient electron-trapping sites, extending carrier lifetimes and enabling multi-electron transfer steps crucial for $CH_4$ generation. Third, the mesoporous structure and large surface area of the composite, as verified by BET analysis, offer abundant $CO_2$ adsorption sites and improved gas diffusion, further accelerating reaction kinetics.

To validate the light-driven nature of the reaction and the involvement of photoinduced charge carriers, several control experiments were performed (**Fig. 4b**). Negligible product formation was observed in the absence of light, under argon atmosphere, or without catalyst, confirming that both light and the photocatalyst are essential. Under visible-light illumination, the system produced 3.96 μmol $g^{-1}$ $h^{-1}$ ($CH_4$) and 5.17 μmol $g^{-1}$ $h^{-1}$ (CO), in line with the optimal photocatalytic performance. The addition of isopropanol (IPA) as a hole scavenger slightly enhanced the yields to 4.45 μmol $g^{-1}$ $h^{-1}$ ($CH_4$) and 5.10 μmol $g^{-1}$ $h^{-1}$ (CO), confirming that photogenerated electrons predominantly drive $CO_2$ reduction while holes are efficiently quenched by IPA [71]. These results substantiate a photoexcitation-driven reduction mechanism, where electrons reduce $CO_2$ to CO and subsequently to $CH_4$, while holes oxidize water molecules to provide protons for hydrocarbon formation.

The durability of the optimal photocatalyst was examined through four consecutive $CO_2$ reduction cycles (**Fig. 4c**). The $CH_4$ yield gradually declined from 3.96 μmol $g^{-1}$ $h^{-1}$ in the first run to 3.81, 2.97, and 1.96 μmol $g^{-1}$ $h^{-1}$ in the subsequent cycles, while CO production decreased from 5.17 μmol $g^{-1}$ $h^{-1}$ to 5.02, 3.87, and 2.23 μmol $g^{-1}$ $h^{-1}$, respectively. This decline is primarily attributed to progressive surface/interfacial deactivation rather than bulk structural degradation. During repeated operation, strongly adsorbed carbonate/bicarbonate species and carbonaceous intermediates can accumulate on the catalyst surface and partially block $CO_2$ adsorption/activation sites, thereby hindering interfacial electron transfer and reducing electron utilization efficiency. In parallel, cyclic photoredox conditions may gradually alter defect-related active centers (e.g., oxygen-vacancy-associated sites and the $Ce^{3+}/Ce^{4+}$ surface balance), leading to fewer effective reduction sites and weaker charge separation across the heterojunction. Minor catalyst loss and mild agglomeration during recovery/washing steps may further reduce accessible surface area [72,73]. Notably, because $CH_4$ formation requires a more demanding multi-electron transfer pathway than CO, it is more sensitive to site blocking and reduced electron availability, explaining the more pronounced decrease in $CH_4$ with cycling [72]. Nonetheless, over 90% of the initial activity was retained after the second cycle, indicating excellent photochemical stability and structural robustness of the 30 wt% $CeVO_4/Bi_2Sn_2O_7$ heterojunction [74,75].

### 3.7. Reactive species and optical properties

To gain deeper insight into the active species governing the photocatalytic degradation of SMX over the 30 wt% $CeVO_4/Bi_2Sn_2O_7$ composite, radical-trapping experiments were initially performed using specific scavengers for different reactive oxygen species (ROS), and the results are shown in **Fig. 4d**. Isopropanol (IPA), *p*-benzoquinone (BQ), and ethylenediaminetetraacetic acid (EDTA) were employed as quenchers for •OH, $•O_2^-$, and $h^+$, respectively. The blank experiment (without scavengers) exhibited a degradation efficiency of 98.18%, confirming the strong intrinsic photocatalytic activity of the optimized composite. Upon the addition of IPA, the efficiency sharply decreased to 26.21%, while the presence of BQ further reduced it to 23.64%, demonstrating that both •OH and $•O_2^-$ radicals play dominant roles in the degradation process. Meanwhile, the degradation efficiency in the presence of EDTA decreased moderately to 80.17%, indicating that photogenerated holes ($h^+$) also participate in the oxidation reactions but to a lesser extent. These results collectively suggest that •OH and $•O_2^-$ radicals are the principal oxidative species responsible for the photocatalytic breakdown of SMX, with holes contributing secondarily to sustaining the oxidation chain.

To further verify the generation of these radicals under visible-light irradiation, ESR spectroscopy was performed using 5,5-dimethyl-1-

pyrroline N-oxide (DMPO) as the spin-trapping agent (Figs. **4e** and **4f**). In the dark, no ESR signals were observed for either DMPO–$\bullet O_2^-$ or DMPO–$\bullet OH$ adducts, confirming the absence of radical species without photoexcitation. Upon visible-light illumination for 10 min, the ESR spectra displayed distinct and intense quadruple peaks characteristic of DMPO–$\bullet O_2^-$ and DMPO–$\bullet OH$ signals, respectively. The strong signal intensity observed under irradiation directly confirms the efficient in-situ generation of both superoxide radicals ($\bullet O_2^-$) and hydroxyl radicals ($\bullet OH$) on the surface of the heterojunction. The simultaneous detection of these active species validates the proposed *Z*-scheme charge-transfer mechanism, wherein the photogenerated electrons in the conduction band of $CeVO_4$ reduce adsorbed $O_2$ molecules to $\bullet O_2^-$ radicals, while the photogenerated holes in the valence band of $Bi_2Sn_2O_7$ oxidize surface-bound $H_2O$ or $OH^-$ to produce $\bullet OH$ radicals [76].

The intrinsic light-harvesting behaviors of the monomers and the electronic band configurations of the individual/composite photocatalysts were clarified by combining the UV–vis spectra of pristine $CeVO_4$ and $Bi_2Sn_2O_7$ (Fig. S3) with the Kubelka–Munk–transformed Tauc analyses (Fig. 4 g–i). As shown in Fig. S3a, $Bi_2Sn_2O_7$ exhibits a steep absorption edge in the near-UV region (around the UV–visible boundary), confirming that its photoresponse is dominated by high-energy photons and that its visible-light absorption is comparatively limited. This trend is consistent with the wider optical band gap extracted from the Tauc plot (Eg = 2.86 eV, Fig. 4 h), which places the fundamental transition close to the UV/visible interface. In contrast, pristine $CeVO_4$ displays a much broader absorption profile extending deep into the visible region (Fig. S3b), evidencing its strong visible-light utilization. The Tauc analysis further quantifies this behavior by giving a narrower band gap of 1.67 eV (Fig. 4 g), which corresponds to a visible-light absorption edge; meanwhile, the long-wavelength tail observed up to ~825 nm in Fig. S3b can be reasonably attributed to sub-bandgap absorption contributions (e.g., defect/oxygen-vacancy-related states, Urbach tailing, and light scattering in the powder), rather than the fundamental band-to-band transition. Importantly, upon coupling $CeVO_4$ with $Bi_2Sn_2O_7$, the 30 wt% $CeVO_4$/ $Bi_2Sn_2O_7$ heterojunction shows an intermediate apparent band gap of 2.43 eV (Fig. 4i), indicating enhanced visible-light harvesting compared with $Bi_2Sn_2O_7$ while maintaining a broader absorption response than the pristine wide-band-gap oxide. This intermediate Eg, together with the complementary absorption features of the two monomers, supports the formation of interfacial electronic coupling in the composite and suggests improved photon utilization and charge excitation under visible irradiation. Consequently, the optical results provide a consistent foundation for the subsequent charge-separation and activity enhancements observed for the heterojunction, as the composite benefits simultaneously from $CeVO_4$'s strong visible-light absorption and $Bi_2Sn_2O_7$'s wide-band-gap framework, yielding more effective photocarrier generation and utilization during photocatalysis.

To further elucidate the electronic band structures, Mott–Schottky (M–S) measurements were performed to determine the flat-band potentials ($E_{fb}$) of $CeVO_4$and $Bi_2Sn_2O_7$. The positive slopes observed in the M–S plots confirm that both photocatalysts possess n-type semiconducting behavior. As illustrated in the insets of Figs. 4 g and 4 h, the flat-band potentials were determined to be approximately 1.15 V vs. NHE for $CeVO_4$ and − 0.60 V vs. NHE for $Bi_2Sn_2O_7$. Considering that, for n-type semiconductors, the conduction band ($E_{CB}$) lies about 0.1 V more negative than $E_{fb}$, the conduction band positions can be estimated as 1.25 eV and − 0.70 eV for $CeVO_4$ and $Bi_2Sn_2O_7$, respectively. The corresponding valence band ($E_{VB}$) potentials, obtained by adding the optical band gap values, are 2.92 eV for $CeVO_4$ and 2.16 eV for $Bi_2Sn_2O_7$. Furthermore, the M–S-derived Fermi levels can be used to clarify the interfacial driving force for charge redistribution: taking $E_{Fb}$ , the effective work functions are $\Phi = 4.44 + E_{fb}$, giving $\Phi$ $CeVO_4$ = 5.59 eV and $\Phi$ $Bi_2Sn_2O_7$ = 3.84 eV. This work-function difference indicates spontaneous electron transfer from $Bi_2Sn_2O_7$ (lower $\Phi$, higher $E_{Fb}$ ) to $CeVO_4$ (higher $\Phi$, lower $E_{Fb}$) upon contact until Fermi-level alignment, establishing interfacial band bending and a built-in electric field that governs directional carrier migration in the heterojunction.

The charge-transfer dynamics and photoelectronic behavior of the photocatalysts were further analyzed using EIS, photoluminescence (PL) spectroscopy, and transient photocurrent response analyses, as shown in **Figs. 4j–4 l**. As illustrated in **Fig. 4j**, the Nyquist plots display semicircular arcs whose diameters represent the charge-transfer resistance ($R_{ct}$) at the electrode–electrolyte interface [77]. Among all samples, 30 wt% $CeVO_4/Bi_2Sn_2O_7$ exhibited the smallest arc radius, indicating the lowest charge-transfer resistance and highest interfacial conductivity [78]. In contrast, pristine $CeVO_4$ and $Bi_2Sn_2O_7$ presented significantly larger semicircles, suggesting more pronounced recombination of photogenerated electron–hole pairs. The reduced $R_{ct}$ in the composite implies that heterojunction formation facilitates faster electron migration and more efficient charge separation, consistent with the *Z*-scheme transfer pathway deduced from band structure analysis [79]. This improved charge transport is critical for enhancing redox reactions during both SMX degradation and $CO_2$ photoreduction.

The PL spectra (**Fig. 4 k**) provide further evidence for the suppression of radiative recombination in the heterostructure. Typically, PL emission results from electron–hole recombination, and a lower PL intensity reflects better charge separation. The emission peaks for all samples appeared near 450 nm, corresponding to the band–band recombination of photoexcited carriers. However, the 30 wt% $CeVO_4/Bi_2Sn_2O_7$ composite exhibited the weakest PL intensity compared with individual $CeVO_4$ and $Bi_2Sn_2O_7$, confirming a substantial decrease in electron–hole recombination probability [80]. This quenching effect arises from efficient charge transfer across the heterojunction interface, facilitated by the favorable band alignment and internal electric field at the $CeVO_4/Bi_2Sn_2O_7$ interface.

Complementarily, the transient photocurrent response measurements (**Fig. 4 l**) demonstrate the photoinduced charge-separation efficiency of the photocatalysts under visible-light illumination. All samples exhibited stable, reproducible photocurrent cycles, confirming their photochemical stability. Notably, the photocurrent density followed the order: 30 wt% $CeVO_4/Bi_2Sn_2O_7$ > $Bi_2Sn_2O_7$ > $CeVO_4$, indicating superior light-driven charge transport in the composite system. The highest photocurrent response of the 30 wt% $CeVO_4/Bi_2Sn_2O_7$ heterojunction underscores its improved photogenerated carrier lifetime and efficient electron transfer, consistent with EIS and PL results.

### 3.8. *Mechanistic insights into charge transfer, $CO_2$ conversion, and SMX degradation*

To elucidate the photocatalytic mechanism of the 30 wt% $CeVO_4$/ $Bi_2Sn_2O_7$ heterojunction, the band alignment derived from UV–Vis DRS and Mott–Schottky (M–S) analyses was correlated with the reactive-species evidence (ESR and scavenger tests) and the photoelectrochemical responses (photocurrent/EIS), as schematically summarized in Fig. 5. In principle, an oxide–oxide junction may operate through a conventional type-II pathway or a direct *Z*-scheme (S-scheme-like) charge-transfer route. However, the experimentally observed simultaneous $CO_2$ reduction (CO and $CH_4$ formation) and strong oxidative degradation of SMX, together with the detected $\bullet OH/\bullet O_2^-$-related activity, are more consistent with a Z-scheme mechanism that preserves high redox capability rather than a redox-attenuating type-II arrangement.

According to the M–S results, both $CeVO_4$ and $Bi_2Sn_2O_7$ exhibit n-type behavior, with flat-band potentials of 1.15 V and − 0.60 V vs NHE, respectively. Using the common n-type approximation that the conduction-band edge is ~0.10 V more negative than Efb, the band edges are estimated as ECB ≈ 1.05 V and EVB ≈ 2.72 V for $CeVO_4$ (Eg = 1.67 eV), and ECB ≈ −0.70 V and EVB ≈ 2.16 V for $Bi_2Sn_2O_7$ (Eg = 2.86 eV). Furthermore, the interfacial driving force can be rationalized by the effective work functions estimated from the M–S-derived Fermi levels (EF ≈ Efb): $\Phi$ $CeVO_4$ ≈ 5.59 eV and $\Phi$ $Bi_2Sn_2O_7$ ≈ 3.84 eV. Upon contact,

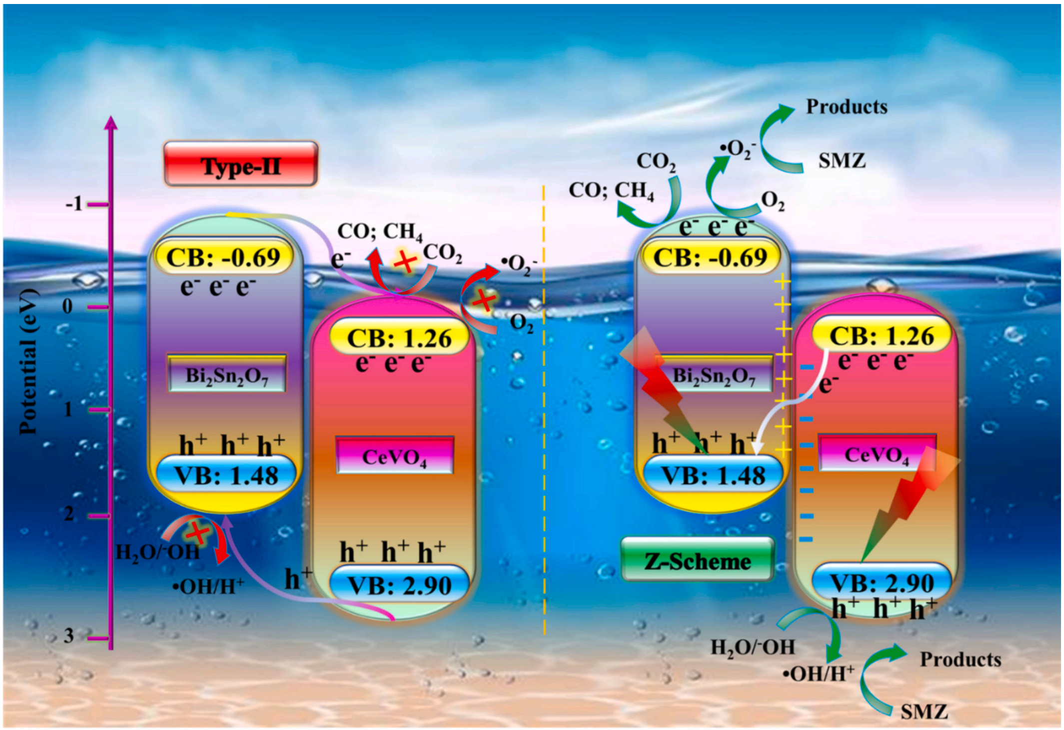

**Fig. 5.** Schematic illustration of the charge-transfer pathways in the $CeVO_4/Bi_2Sn_2O_7$ heterojunction under visible-light irradiation, comparing the conventional type-II route and the revised direct Z-scheme mechanism.

electrons spontaneously transfer from $Bi_2Sn_2O_7$ (lower Φ, higher EF) to $CeVO_4$ (higher Φ, lower EF) until Fermi-level equilibration, establishing interfacial band bending and a built-in electric field that promotes directional charge separation across the heterojunction [81].

If a conventional type-II pathway dominated, photogenerated electrons would preferentially accumulate in the less negative conduction band and holes in the less positive valence band, which would diminish the intrinsic redox power. With the present band edges, electron accumulation in the $CeVO_4$ conduction band (ECB ≈ 1.05 V vs NHE) would be thermodynamically incapable of driving $CO_2$ reduction ($E^0(CO_2/CO) = -0.53$ V; $E^0(CO_2/CH_4) = -0.24$ V vs NHE), while hole accumulation in the $Bi_2Sn_2O_7$ valence band (EVB ≈ 2.16 V) would be insufficient to generate •OH from $H_2O$ ($E^0(\bullet OH/H_2O) = 2.27$ V). Therefore, a type-II mechanism cannot account for the experimentally observed $CO/CH_4$ production together with strong •OH-involved oxidation activity.

In the revised direct *Z*-scheme mechanism (Fig. 5), both semiconductors are photoexcited under visible-light irradiation. At the interface, the built-in electric field and band bending facilitate selective recombination between the relatively weak carriers, namely electrons in the $CeVO_4$ conduction band and holes in the $Bi_2Sn_2O_7$ valence band. This interfacial recombination retains the strongly reducing electrons on $Bi_2Sn_2O_7$ (ECB ≈ −0.70 V) and the strongly oxidizing holes on $CeVO_4$ (EVB ≈ 2.72 V), thereby preserving high redox capability while suppressing bulk recombination—consistent with the enhanced photoelectrochemical behavior of the heterojunction [82].

On the reduction side, $CO_2$ molecules adsorbed on the catalyst surface are activated and reduced by electrons accumulated in the $Bi_2Sn_2O_7$ conduction band (ECB ≈ −0.70 V), which is sufficiently negative to drive CO formation and, under favorable proton/electron availability, deeper hydrogenation toward $CH_4$. The corresponding half-reactions can be expressed as: $CO_2 + 2H^+ + 2e^- \rightarrow CO + H_2O$ ($E^0 = -0.53$ V) and $CO_2 + 8H^+ + 8e^- \rightarrow CH_4 + 2H_2O$ ($E^0 = -0.24$ V vs NHE). In addition, dissolved $O_2$ can scavenge electrons to form $\bullet O_2^-$ ($O_2 + e^- \rightarrow \bullet O_2^-$, $E^0 = -0.33$ V), which contributes to oxidative pathways and further suppresses electron–hole recombination.

On the oxidation side, holes preserved on the $CeVO_4$ valence band (EVB ≈ 2.72 V) possess sufficient oxidizing power to produce hydroxyl radicals via $H_2O/OH^-$ oxidation ($H_2O + h^+ \rightarrow \bullet OH + H^+$, $E^0 = 2.27$ V; $OH^- + h^+ \rightarrow \bullet OH$, $E^0 = 1.99$ V). The generated •OH, together with $\bullet O_2^-$ and direct hole oxidation, serves as the primary oxidative ensemble responsible for SMX degradation, consistent with the ESR and radical-trapping results. These reactive species initiate successive bond cleavage and ring-opening reactions, ultimately transforming SMX into low-molecular-weight intermediates and mineralization products ($CO_2$ and $H_2O$). Overall, the $CeVO_4$/ $Bi_2Sn_2O_7$ heterojunction functions as an interfacial electric-field-assisted *Z*-scheme system that simultaneously sustains strong reduction activity for $CO_2$ conversion on $Bi_2Sn_2O_7$ and strong oxidation activity for SMX degradation on $CeVO_4$, thereby rationalizing the dual-function photocatalytic performance.

## 4. Conclusions

In summary, a novel Z-scheme $CeVO_4/Bi_2Sn_2O_7$ heterojunction was successfully fabricated via a facile hydrothermal–ultrasonication method. Comprehensive characterization using XRD, XPS, SEM/TEM, and BET analysis confirmed the successful formation of the heterostructure with intimate interfacial contact, a high surface area, and a mixed-valence defect-rich surface. This unique architecture was instrumental in establishing a direct Z-scheme charge-transfer pathway, as verified by ESR and photoelectrochemical analyses, which drastically enhanced the spatial separation of photogenerated electron-hole pairs while preserving their high redox potentials. The optimized 30 wt% $CeVO_4/Bi_2Sn_2O_7$ composite exhibited remarkable dual-functional activity. It achieved $CO_2$ conversion rates of 3.96 μmol $g^{-1}$ $h^{-1}$ for $CH_4$ and 5.17 μmol $g^{-1}$ $h^{-1}$ for CO, representing a 19.8-fold and 11.5-fold enhancement, respectively, over pristine $CeVO_4$. Simultaneously, it demonstrated superior photocatalytic degradation, removing 98.18% of SMX under visible light. The process ensured deep mineralization (81.46% TOC removal), and toxicity assessments confirmed the effective detoxification of SMX. The catalyst also displayed remarkable versatility against various antibiotics and maintained robust performance in different water matrices, including real wastewater. Furthermore, the composite exhibited excellent photostability and reusability over multiple cycles. DFT calculations provided fundamental insights into the SMX degradation pathways, aligning perfectly with the proposed Z-scheme mechanism. Collectively, this work presents the $CeVO_4/Bi_2Sn_2O_7$ Z-scheme heterojunction as a highly efficient, stable, and versatile photocatalyst with significant potential for addressing the dual challenges of environmental remediation and renewable energy production.

## CRediT authorship contribution statement

**Rahila Batul:** Data curation, Formal analysis, Funding acquisition, Investigation, Software, Validation, Writing – review & editing. **Ali B.M. Ali:** Data curation, Formal analysis, Funding acquisition, Investigation, Software, Validation, Writing – review & editing. **Mohamed A. Ismail:** Writing – review & editing, Validation, Resources, Methodology, Funding acquisition, Formal analysis, Data curation, Conceptualization. **Pradeep Kumar Singh:** Supervision, Conceptualization, Writing – original draft, Methodology, Investigation. **Shatha A. Aldaghfag:** Data curation, Formal analysis, Funding acquisition, Investigation, Software, Validation, Writing – review & editing. **Ibrahm Mahariq:** Data curation, Formal analysis, Funding acquisition, Investigation, Software, Validation, Writing – review & editing. **Bakhodir Saydullaev:** Data curation, Formal analysis, Funding acquisition, Investigation, Software, Validation, Writing – review & editing. **Miyribek Seytnazarov:** Data curation, Formal analysis, Funding acquisition, Investigation, Software, Validation, Writing – review & editing. **Mukhtorjon Karimov:** Data curation, Formal analysis, Funding acquisition, Investigation, Software, Validation, Writing – review & editing. **Reda A. Haggam:** Data curation, Formal analysis, Funding acquisition, Investigation, Software, Validation, Writing – review & editing.

## Fundings

This research was funded by the Deanship of Research and Graduate Studies at King Khalid University under grant number RGP.2/431/46. The authors also express their gratitude to Princess Nourah bint Abdulrahman University Researchers Supporting Project number (PNURSP2026R81), Princess Nourah bint Abdulrahman University, Riyadh, Saudi Arabia

## Declaration of competing interest

The authors declare that they have no known competing financial interests or personal relationships that could have appeared to influence the work reported in this paper.

## Acknowledgments

The authors extend their appreciation to the Deanship of Research and Graduate Studies at King Khalid University for funding this work through Large Group Project under grant number RGP.2/431/46. The authors also express their gratitude to Princess Nourah bint Abdulrahman University Researchers Supporting Project number (PNURSP2026R81), Princess Nourah bint Abdulrahman University, Riyadh, Saudi Arabia.

## Appendix A. Supplementary data

Supplementary data to this article can be found online at https://doi.org/10.1016/j.seppur.2026.137266.

## Data availability

No data was used for the research described in the article.

## References

[1] S. Shang, Y. Wei, X. Zhao, W. Wang, S. An, H. Li, C. Peng, H. Liu, H. Chen, J. Hu, Dimensional engineering of 1D/2D covalent organic framework isomers for enhanced $CO_2$ photoreduction, Small 21 (2025) e06081.

[2] P. Cao, M. Long, X. Zheng, C. Zhou, Y. Chen, B.E. Rittmann, Selective regulation of product generation from CO2 hydrogenation on Pd-based catalysts: a critical review from a pathway perspective, Energy Environ. Sustainability 1 (2025) 100020.

[3] Z. Fang, H. Ma, H. Shao, W. Dai, Z. Qu, S. Liu, Y. Xue, S. Xiao, Enhanced $CO_2$ photoreduction to methane via Schottky $Zn_3N_2$/KPCN heterojunctions for sustainable energy applications, Environ. Res. 268 (2025) 120740.

[4] H. Chi, Y. Leng, C. Ding, T. Li, Y. Zhang, J. Yuan, W. Tu, W. Gao, Y. Yao, X. Zhu, Y. Zhou, Z. Zou, Spin polarization-boosting ultrafast carrier dynamics and exciton dissociation in Fe nanoparticle-loading graphitic carbon nitride toward efficient CO2 photoreduction, Angew. Chem. Int. Ed. 64 (2025) e202425630.

[5] Y. Wang, J. Hu, F. Chen, S. Wang, Y. Lu, H. Huang, Ferroelectric polarization tailoring of cu single atoms: modulating d-band and basic sites for efficient $CO_2$ photoreduction, Appl. Catal. B Environ. Energy 382 (2026) 125966.

[6] K. Rasouli, J. Rasouli, M.S. Mohtaram, S. Sabbaghi, H. Kamyab, H. Moradi, S. Chelliapan, Biomass-derived activated carbon nanocomposites for cleaner production: a review on aspects of photocatalytic pollutant degradation, J. Clean. Prod. 419 (2023) 138181.

[7] A.S. Elkomy, M.Sh. Abdel-wahab, N. Shehata, A comparison between adsorption and photocatalytic degradation for the management of sulfamethoxazole in water, Sci. Rep. 15 (2025) 13576.

[8] Y. Jia, L. Duan, H. Li, C. Zhang, Q. Gao, H. Zhang, S. Li, M. Li, Visible light activation of persulfate by α-Fe2O3/PDINH photocatalyst for sulfamethoxazole degradation, Sep. Purif. Technol. 354 (2025) 129287.

[9] S. Fu, S. Tao, C. Zhang, D. Zhou, Near-complete mineralization of sulfamethoxazole through intimately coupled Fe2O3/Mn2O3-catalytic ozonation and biodegradation with low ozone dosage, J. Clean. Prod. 520 (2025) 146098.

[10] N. Geng, L. Yang, Y. Wang, C. Huang, G. Geng, L. Chen, K. Sun, T. Liu, High efficiency sulfamethoxazole degradation enabled by chlorinated D–A scheme organic photocatalysts, J. Mater. Chem. C 13 (2025) 11448–11459.

[11] Y. Li, Z. Cheng, H. Shang, Y. Chen, S. Li, X. Wei, T. Wang, W. Zhou, Y. Yu, Design of functional groups on biochar for sulfamethoxazole adsorption from adsorption efficiency and adsorption mechanism, J. Environ. Chem. Eng. 13 (2025) 116874.

[12] X. Yan, Z. Pan, G. Feng, R. Xu, L. Li, S. Zhao, X. Fan, C. Song, T. Wang, CuOx-coated titanium hollow fiber electrocatalytic membrane for efficient sulfamethoxazole removal: preparation, performance and degradation mechanism, J. Membr. Sci. 731 (2025) 124211.

[13] S. Li, S. Yan, Z. Tong, X. Yong, X. Zhang, J. Zhou, Assessment of photocatalytic activities of layered double hydroxide@petrochemical sludge biochar for sulfamethoxazole degradation, Sep. Purif. Technol. 355 (2025) 129732.

[14] Z. Chen, J. Li, J. Zhang, H. Wang, Y. Zeng, F. Wang, P. Huang, X. Chen, L. Ge, R. A. Dahlgren, H. Gao, X. Huang, A highly efficient and recyclable living biocatalyst using Shewanella@polydopamine@NH2-doped carbon dot biohybrids and polypyrrole immobilized melamine foam for microbial-photoreduction of Cr(VI), J. Clean. Prod. 435 (2024) 140497.

[15] F. Jiang, Y. Zhang, X. Xu, Y. Mao, M. Wang, B. Yang, C. Zhang, X. Feng, H. Meng, F. Guo, Q. Han, S. Zhang, Application of cysteine with Cu2+ to strengthen Fenton-based treatment of coking wastewater used ferric sludge as a source of iron catalyst: Cl- removal and Fe3+/Fe2+ cycling, J. Environ. Chem. Eng. 13 (2025) 117556.

[16] Y. Song, Z. Li, C. Yang, X. Wen, L. Huang, X. Zhang, Y. Ma, Q. Wang, H. Zhang, Novel construction of Z–scheme g–C3N4/PDI organic photocatalyst for excellent sulfamethoxazole degradation rate in water, J. Environ. Chem. Eng. 13 (2025) 118371.

[17] J. Zhao, A.B.M. Ali, A.A.H. Kadhum, H. Lin, A.S. Abdelhameed, A.M. Alanazi, I. Mahariq, E. Khudoynazarov, D. Jumanazarov, F. Atamurotov, Boosting photocatalytic H2O2 production and non-biodegradable ofloxacin removal via a novel Ti3C2 MXene nanosheet-supported BiVO4/InVO4 Z-scheme heterojunction: optimization and mechanism insights, J. Water Process Eng. 74 (2025) 107722.

[18] W. Wang, M. Xu, J. Sun, K. Zuo, X. Wang, J. Lan, L. Yang, S. Wang, Y. Ren, Novel g-C3N4-x nanosheets/MoS2 binary photocatalyst achieves stable construction of Z-scheme heterojunction via nitrogen defect induced 2D interface C-S bonds for efficient PMS activation and degradation of sulfamethoxazole, Environ. Res. 279 (2025) 121888.

[19] J. Wang, J. Zhang, G. Cheng, K. Zhang, X. Liu, Performance and mechanism of tetracycline removal by peroxymonosulfate-assisted double Z-scheme LaFeO3/g-C3N4/ZnO heterojunction under visible light drive, Environ. Technol. Innovation 39 (2025) 104302.

[20] Y. Lu, Y. Zhao, S. Wang, B. Hu, Exploring charge-transfer of 2D borophene in carbon nitride: boosting uranium photoreduction, Desalination 619 (2026) 119488.

[21] R. Li, B. Wang, Y. Zhao, N. Zhang, X. Zhao, Z. Gao, H. Guo, H. Wang, In-situ growth of WO3/Bi2WO6 heterojunctions on carbon fiber cloth: design, morphology modulation and photocatalytic performance, J. Environ. Chem. Eng. 13 (2025) 118926.

[22] J. Zou, L. Li, N. Tan, K. Zhang, L. Wang, Z. Chen, Construction of S-scheme heterojunction with interfacial chemical bonds for enhanced photocatalytic CO2 reduction, Appl. Surf. Sci. 719 (2026) 165001.

[23] J. Huang, K. Rasouli, Z. Zong, P. Wang, Y. Zhang, Z. Li, Engineering a high-performance ZnFe2O4/BiOBr/MXene S-scheme heterostructure for CO2

photoreduction and wastewater treatment, Chemical Engineering Journal 530 (2026) 173675.

[24] R. Fiorenza, L. Calantropo, E. La Greca, L.F. Liotta, A. Gulino, A. Ferlazzo, M. G. Musumeci, G. Proietto Salanitri, S.C. Carroccio, G. Dativo, M.T. Armeli Iapichino, S. Scirè, G. Impellizzeri, Solar-promoted photo-thermal CO2 methanation on SiC/hydrotalcites-derived catalysts, Catal. Today 449 (2025) 115182.

[25] W. Shen, X. Gao, Q. Liu, P. Li, R. Huang, Y. Tan, Z. Wang, Y. Zhang, F. Zhao, X. Wang, S. Ji, X. Zheng, Y. Zhang, Y. Wu, Self-healing Cu single-atom catalyst for high-performance electrocatalytic CO2 methanation, Nat. Commun. 16 (2025) 7943.

[26] C. Chen, S. Du, Y. Wang, Z. Han, S. Zhang, W. Ma, H. Xu, P. Fang, Hollow MoSe2/N-doped carbon composited with ZnIn2S4 constructing dual Z-scheme heterojunction for enhanced visible-light photocatalytic performances, J. Colloid Interface Sci. 701 (2026) 138758.

[27] Z. He, K. Lin, N. Hing Wong, J. Sunarso, Y. Xia, X. Fu, J. Su, Z. Huang, Y. Wang, B. Tang, Elucidation of mechanisms, pathways, and toxicity of fabricated Z-scheme KNbO3/ZnIn2S4 hollow core–shell composites for enhanced ciprofloxacin photodegradation, Chem. Eng. J. 475 (2023) 146262.

[28] Y. Xia, Z. He, G. He, L. Chen, J. Zhang, J. Su, M.S. Siddique, X. Fu, G. Chen, W. Zhou, Lead-free perovskite Cs3Bi2Br9/FeS2 hollow core-shell Z-scheme heterojunctions toward optimized photothermal-photocatalytic H2 production, Chin. Chem. Lett. 36 (2025) 111521.

[29] Z. Liu, J. Liu, J. Wang, P. Lu, S. Xu, Y. Lu, X. Li, Q. Zhang, G. Jiang, Z. Li, Cs3Bi2Br9/Bi19Br3S27 Z-scheme heterojunction for visible-to-near-infrared light-driven photocatalytic CO2 reduction, J. Colloid Interface Sci. 699 (2025) 138238.

[30] Z. He, Y. Xia, F. Wang, J. Su, N. Hing Wong, J. Sunarso, X. Fu, G. Chen, H. Yang, W. Zhou, Rationally designed photothermal-pyroelectric Fe0.9Ni0.1S2/ZnSnO3 Z-scheme heterojunction for promoting electrical charge polarization towards optimized photocatalytic H2 evolution and intermolecular N-N coupling reaction, Sep. Purif. Technol. 357 (2025) 130201.

[31] S. Li, H. Lin, X. Jia, Q. Wang, H. Zhang, Y. Zhang, X. Feng, S. Chen, J. Cao, Z-scheme heterojunction with spatially separated dual redox-active sites for coupled carbon dioxide photoreduction and tetracycline photooxidation, J. Colloid Interface Sci. 699 (2025) 138218.

[32] Z. He, K. Lin, N.H. Wong, J. Sunarso, Y. Xia, X. Fu, B. Tang, Z. Huang, Y. Wang, H. Yang, Electron spin-states reconfiguration induced by alternating temperature gradient for boosting photocatalytic hydrogen evolution on hollow core-shell FeS2/CuCo2O4 Z-scheme heterostructure, Nano Energy 124 (2024) 109483.

[33] Z. He, Y. Xia, F. Wang, J. Su, M.S. Siddique, X. Fu, G. Chen, H. Yang, W. Zhou, Promising CdS quantum dots/FeS2 microsphere Z-scheme heterojunction for boosting C-C coupling and hydrogen production, J. Clean. Prod. 501 (2025) 145361.

[34] M. Wang, Q. Gao, Y. Chai, R. Zhang, Z. Liu, Y. Zhu, Construction of Z−scheme Bi2MoO6/CeVO4 nanofibers heterojunctions with enhanced visible−light−driven photocatalytic activity, J. Alloys Compd. 1036 (2025) 182150.

[35] C. Zheng, T. Li, Y. Wang, Y. Wu, J. Wu, F. Yu, C. Lu, Y. Xie, Efficient photocatalytic hydrogen evolution via S-scheme CdSe/CeVO4 heterojunction with in situ XPS validated charge transfer mechanism, J. Environ. Chem. Eng. 13 (2025) 116958.

[36] J. Hua, F.-Y. Chen, Y.-B. Tang, S.-G. Zhao, X.-G. Wang, W.-Q. Sun, J.-T. Yang, Fabrication of a novel Z-scheme p-n heterojunction photocatalyst 0D/3D CeVO4/MIL-88(A): enhanced photocatalytic performance and mechanism insight, J. Phys. Chem. Solids 207 (2025) 112969.

[37] A.Ç. Yıldız, S. Çakar, CeVO4/TiO2/SnS based nanostructured ternary photoelectrode and photocatalyst for photoelectrochemical O2 and photocatalytic H2 evolution by solar energy, Inorg. Chem. Commun. 179 (2025) 114706.

[38] S.R. Mishra, S. Rawat, R.S. Pawar, R.R. Nikam, S. Roy, V. Gadore, M. Ahmaruzzaman, B.M. Nagaraja, Double Z-scheme bifunctional In2S3-CeVO4-La2O3 ternary heterostructure for enhanced photocatalytic application, Surfaces and Interfaces 75 (2025) 107810.

[39] J. Liu, L. Zhen, Y. Xu, J. Liu, Z. Liu, Z. Zhang, J. Shi, H. Deng, Efficient activation of Fe-Bi2Sn2O7 for pollutant removal by peroxodisulfate: synergistic Fenton-like and photoreactions, Sep. Purif. Technol. 373 (2025) 133613.

[40] F. Tian, Y. Li, W. Miao, J. Liang, D.V.C. Rodríguez, X. Yan, Internal electric field-modulated charge migration behavior in atom co-sharing Bi2S3/Bi2Sn2O7 heterojunction for efficient tetracycline degradation, Surf. Interfaces 62 (2025) 106280.

[41] C. Jiang, S. Zhang, S. Chen, X. Yao, H. Ji, Y. Tong, Preparation of Z-scheme AgI/Bi2Sn2O7 hybrids for profound CC/CO bonds cleavage in lignin β-O-4 ketone models, J. Colloid Interface Sci. 686 (2025) 430–437.

[42] X. Liu, Y. Su, Y. Li, Q. Ma, J. Luo, Accompanying Bi clusters as charge mediators effectively enhance synergetic redox of Bi2Sn2O7/ZnIn2S4 S-scheme Heterostructure composites, Small 21 (2025) 2410721.

[43] N.S. Mishra, A. Kuila, P. Saravanan, D. Bahnemann, M. Jang, S. Routu, Simultaneous S-scheme promoted Ag@AgVO3/g-C3N4/CeVO4 heterojunction with enhanced charge separation and photo redox ability towards solar photocatalysis, Chemosphere 326 (2023) 138496.

[44] N.S. Mishra, P. Saravanan, Z-scheme promoted heterojunction photocatalyst (Ag@AgVO3 /rGO/CeVO4) with improved interfacial charge transfer for efficient removal of aqueous organics irradiated under LED light, Chemosphere 310 (2023) 136896.

[45] D. Fayazi, A. Dolatimehr, A. Teymoori, S. Khalili, N.M. Vaziri, Z. Khaksar, Uniform dispersion of Bi2Sn2O7 nanoparticles on intersectional CuO monolayers for levofloxacin photodegradation: exploring influence of morphology on S-type charge migration, J. Water Process Eng. 77 (2025) 108626.

[46] S.-H. Guo, R.-T. Guo, Z.-R. Zhang, L.-Q. Yu, J.-S. Yan, H. Liu, Highly selective conversion of CO2 to C2H6 by photocatalytic reduction with NiAl–layered double hydroxides/Bi2Sn2O7–Ov/CuO–Ov double oxygen vacancy photocatalyst, Sol. RRL 9 (2025) 2400820.

[47] K. Rasouli, A. Alamdari, S. Sabbaghi, Ultrasonic-assisted synthesis of α-Fe2O3@TiO2 photocatalyst: optimization of effective factors in the fabrication of photocatalyst and removal of non-biodegradable cefixime via response surface methodology-central composite design, Sep. Purif. Technol. 307 (2023) 122799.

[48] J. Rasouli, A. Zandifar, K. Rasouli, S. Sabbaghi, F. Esmaeilzadeh, M. Shah, K. B. Ansari, High-efficiency ternary CeO2/WO3/AC photocatalyst supported by biomass waste-derived activated carbon for efficient doxycycline photodegradation: optimization of synthesis conditions and operational parameters, Mater. Res. Bull. 178 (2024) 112874.

[49] Y. Gan, D. Zeng, S. Ning, N. Zheng, X. Wang, Y. Wei, J. Jiang, Synergistic H2 production and tetracycline degradation: Unveiling the mechanism of a one-pot synthesized CeO2/CdS photocatalyst, Chinese Chemical Letters 37 (2026) 111717.

[50] M. Cheng, H. Li, Z. Wu, Z. Yu, X. Tao, L. Huang, Synergistic effects of CQDs and oxygen vacancies on CeO2 photocatalyst for efficient photocatalytic nitrogen fixation, Sep. Purif. Technol. 354 (2025) 129299.

[51] P. Zhang, Q. Wu, H. Wang, D.-H. Kuo, Y. Lai, D. Lu, J. Li, J. Lin, Z. Yuan, X. Chen, Z-scheme heterojunction Zn3(OH)2(V2O7)(H2O)2/V-Zn(O,S) for enhanced visible-light photocatalytic N2 fixation via synergistic heterovalent vanadium states and oxygen vacancy defects, Chin. J. Catal. 74 (2025) 279–293.

[52] L. Wang, J. Zhao, Organic/inorganic composite S-scheme photocatalyst with enhanced light absorption and H2O2-production activity, J. Mater. Sci. Technol. 241 (2026) 18–20.

[53] R. Bai, J. Niu, X. Zhang, Q. Li, C. Dong, Q. Shen, J. Xue, Y. Zhu, Enhanced photocatalytic CO2 reduction in floatable CMF/Bi2WO6/C3N4 gas-liquid-solid three-phase heterojunction system, Appl. Catal. B Environ. Energy 374 (2025) 125395.

[54] C.E. Choong, K. Hong, K.T. Wong, Z.Y. Kong, A. Yang, F. Mohd Jais, Y. Yoon, E. H. Choi, M. Jang, Overlooked roles of high-valence Sn in SnS2 loaded on gC3N4 for enhanced photocatalytic H2O2 production: mechanism, DFT, and techno-economic analysis study, J. Energy Chem. 108 (2025) 154–164.

[55] M. Boujelbene, A.B.M. Ali, K. Alsaikhan, A. BaQais, M.B.B. Hamida, A. Amari, Y. Yusupov, A. Abduvokhidov, E. Khudoynazarov, Enhanced photocatalytic performance for organic pollutants degradation and H2O2 production using a novel rGO-bridged $Bi_2MoO_6$-$CoTiO_3$ Z-scheme composites: analytical characterization, mechanism and toxicity assessment, Surf. Interfaces 72 (2025) 107201.

[56] Y. Pajouhan, S. Sabbaghi, K. Rasouli, J. Rasouli, W. Dastyar, E. Andiroglu, Enhanced photocatalytic degradation of tetracycline using α-Fe2O3@TiO2-impregnated Mxene photocatalyst: mechanism and optimization of process via RSM and ANN, Process. Saf. Environ. Prot. 190 (2024) 1149–1163.

[57] K.I.S. Mabape, S.B. Mishra, M.J. Moloto, A.K. Mishra, Visible light enhanced degradation of sulfamethoxazole by Beta Zeolite/TiO2 photocatalyst, ChemistrySelect 10 (2025) e00680.

[58] M. Rostami, A. Badiei, G.M. Ziarani, M. Fasihi-Ramandi, M. Jourshabani, B.K. Lee, M. Rahimi-Nasrabadi, F. Ahmadi, C3N5-Cu-doped Co3O4 @NPC nano-cubes heterojunction architecture for sono-photocatalytic degradation of the antibiotic sulfamethoxazole, electrocatalysis water splitting for HER, and cytotoxic performance, J. Ind. Eng. Chem. 151 (2025) 591–604.

[59] X. Bai, X. Liu, R. Zong, Enhancement of photocatalytic self-Fenton degradation toward sulfamethoxazole by highly symmetrical triazine-based covalent organic frameworks, Appl. Catal. B Environ. Energy 366 (2025) 125062.

[60] A. Majumder, P. Mandal, M.K. Yadav, A.L. T, L. B, A. Majumder, Machine learning-powered estimation of simultaneous removal of sulfamethoxazole, 17-β estradiol, and carbamazepine via photocatalytic degradation with M-Al@ZnO, Environ. Res. 286 (2025) 122989.

[61] L.C. Fabris, A.C. Ferreira Piazzi Fuhr, F.M. Machado, A. Swarowsky, E.L. Foletto, D. M. Souza, E. Carissimi, J. Leichtweis, Rice husk waste biochar as a photocatalyst support for use in the degradation of organic pollutants, Chemical Engineering Science 325 (2026) 123497.

[62] M.S. Mohtaram, S. Sabbaghi, J. Rasouli, K. Rasouli, Photocatalytic degradation of tetracycline using a novel WO3–ZnO/AC under visible light irradiation: optimization of effective factors by RSM-CCD, Environ. Pollut. 347 (2024) 123746.

[63] J. Rasouli, M. Binazadeh, S. Sabbaghi, Synthesis of a novel biomass waste-based photocatalyst for degradation of high concentration organic pollutants under visible light: optimization of synthesis condition and operational parameters via RSM-CCD, Surf. Interfaces 49 (2024) 104400.

[64] M.H. Abdallah, A.B.M. Ali, M.K. Kareem, P.K. Singh, M. Hasan, E. Khudoynazarov, E. Saitov, D. Jumanazarov, I. Mahariq, R.A. Haggam, Efficient Z-scheme NiTiO3–Zn3V2O8 photocatalyst for visible-light-driven antibiotic degradation and H2O2 production: characterization, mechanistic insights, and toxicity assessment, Surf. Interfaces 80 (2026) 108208.

[65] Y. Jia, L. Duan, H. Li, C. Zhang, Q. Gao, H. Zhang, S. Li, M. Li, Fast removal of sulfamethoxazole by MIL-101(Fe)–NH2/perylene diimide activated persulfate under visible light, Sep. Purif. Technol. 358 (2025) 130292.

[66] C. Tang, B. Lin, H. Niu, K. Zheng, Y. Liu, X. Chen, K. Zhong, R. Zhu, Y. Chen, H. Li, Y. Wu, Y. Huang, X. Yuan, Highly dispersed ZIF-67 derived cobalt nanoparticle supported on g-C3N4 for rapid degradation of sulfamethoxazole by Fenton-like oxidation: enhanced adsorption and electron transfer, J. Colloid Interface Sci. 698 (2025) 138062.

[67] T. Zhu, G. Li, Y. Cheng, H. Li, M. Zhou, M. Jing, Potential and degradation mechanism of sulfamethoxazole removal by the synergistic effect of micro-nano bubbles and sodium hypochlorite, Environ. Geochem. Health 47 (2025) 393.

[68] F. Meng, C. Qu, L. Wang, D. Yang, Z. Zhao, Q. Ye, ZIF-67-derived NiCo2O4 hollow nanocages coupled with g-C3N4 nanosheets as Z-scheme photocatalysts for enhancing CO2 reduction, J. Colloid Interface Sci. 684 (2025) 492–502.

[69] M. Zha, F. Wang, H. Sun, S. Yao, H. Wang, L. Liu, Construction of ZIS/CdS Z-scheme heterojunction for enhanced CO2 photoreduction to CO, Sep. Purif. Technol. 376 (2025) 133886.

[70] Y. Song, Y. Song, X. Li, R. Wang, S. Sun, Q. Jiang, H. Song, W. Lin, W. Lin, Defect engineering of Z-scheme heterojunction catalysts for efficient CO2 photoreduction, Chem. Eng. J. 513 (2025) 162800.

[71] C. Tang, T. Bao, S. Li, X. Li, H. Rao, P. She, J.-S. Qin, Rapid charge transfer endowed by hollow-structured Z-scheme heterojunction for coupling benzylamine oxidation with CO2 reduction, Adv. Funct. Mater. 35 (2025) 2415280.

[72] P.M. Gawal, A.K. Golder, Novel ternary Z-scheme nanocomposites: biomass-derived carbon dots decorated on g-C3N4(Thiourea) -g-C3N4(urea) heterostructures for photocatalytic CO2 reduction to CO and H2, Int. J. Hydrog. Energy 199 (2026) 152856.

[73] Y. Zhou, P. Cao, H. Bai, M.I. Ahmad, S. Chen, Y. Liu, H. Yu, X. Quan, Lewis acid-base dual sites promote sacrificial agent-free photocatalytic CO2 reduction to ethanol, Appl. Catal. B Environ. Energy 380 (2026) 125780.

[74] Z. Yuan, J. Liu, Y. Xiang, X. Jian, H. Zhang, M. Liu, R. Cao, Y. Hu, X. Gao, Activation of Bi2MoO6/Zn0.5Cd0.5S charge transfer through interface chemical bonds and surface defects for photothermal catalytic CO2 reduction, J. Colloid Interface Sci. 677 (2025) 482–493.

[75] M. Khan, Z. Akmal, M. Tayyab, S. Mansoor, M.A. Zeb, A. Zeeshan, M.M. Khan, Z. Ye, J. Zhang, S. Wu, L. Wang, Engineering spatially proximate redox sites in Pd-In/TiO2 photocatalyst for selective CO2 photoreduction, Appl. Surf. Sci. 709 (2025) 163644.

[76] L. Li, K. Zheng, Z. Li, Z. Chen, W18O49/ZnIn2S4 S-scheme photocatalyst with full-spectrum response for efficient H2O2 production, J. Mater. Sci. Technol. 245 (2026) 309–321.

[77] N.S. Sawaran Singh, A.B.M.. Ali, M. Shah, M.K. Al Mesfer, A. Abduvokhidov, A. Abilkasimov, D. Jumanazarov, E. Davletov, M.A. Diab, High-performance visible-light photocatalyst based on IL-modified Bi2MoO6 with MXene charge mediation and MIL-100(Fe) adsorptive oxidation for broad-spectrum aqueous remediation, Surf. Interfaces 76 (2025) 107929.

[78] L. Zhang, J. Zhang, J. Yu, H. García, Charge-transfer dynamics in S-scheme photocatalyst, Nat. Rev. Chem. 9 (2025) 328–342.

[79] M. Boujelbene, A. Basem, N.S. Alsaiari, S.A. Aldaghfag, M.A. Ismail, W. Rajhi, S. Ibragimova, A. Abilkasimov, Z. Atamuratova, Solar-driven dual-functional Z-scheme ZnIn2S4–Sb2O3 supported on activated carbon for simultaneous H2 generation and norfloxacin degradation: mechanism, analytical characterization, and toxicity assessment, Surf. Interfaces 75 (2025) 107785.

[80] T. Sun, K. Wang, Y.-X. Du, J.-G. Chen, X.-P. Li, Z.-H. He, X. Hao, W. Wang, H. Wang, Z.-T. Liu, Synergistic spin-polarization and ohmic contact in Co2 + doped ultrathin BiOCl nanosheets with Bi sub-nanoclusters for boosted CO2 photoreduction, Appl. Catal. B Environ. Energy 381 (2026) 125849.

[81] Y. Xia, Z. He, G. He, X. Chen, J. Zhang, F. Wang, Y. Hartanto, J. Sunarso, F. Gapsari, G. Chen, X. Fu, H. Yang, Pd single-atom and S-scheme heterojunction synergy in improving charge transport for high performance photocatalyzed hydrogen evolution reaction, Sep. Purif. Technol. 372 (2025) 133480.

[82] Z. He, H. Fareed, H. Yang, Y. Xia, J. Su, L. Wang, L. Kang, M. Wu, Z. Huang, Mechanistic insight into the charge carrier separation and molecular oxygen activation of manganese doping BiOBr hollow microspheres, J. Colloid Interface Sci. 629 (2023) 355–367.